Stony Brook University

OFFICIAL COPY

The official electronic file of this thesis or dissertation is maintained by the University Libraries on behalf of The Graduate School at Stony Brook University.

© All Rights Reserved by Author.

Development of Type-I GaSb-based Diode Lasers and Arrays Operating within Spectral Range above 2μm

A Dissertation Presented

by

Jianfeng Chen

to

The Graduate School

in Partial Fulfillment of the

Requirements

for the Degree of

Doctor of Philosophy

in

Electrical Engineering

Stony Brook University

May 2011

Stony Brook University

The Graduate School

Jianfeng Chen

We, the dissertation committee for the above candidate for the

Doctor of Philosophy degree, hereby recommend

acceptance of this dissertation.

Leon Shterengas – Dissertation Advisor
Assistant Professor, Department of Electrical & Computer Engineering

Ridha Kamoua - Chairperson of Defense
Associate Professor, Department of Electrical & Computer Engineering

Dmitri Donetski
Associate Professor, Department of Electrical & Computer Engineering

Thomas Cubaud
Assistant Professor, Department of Mechanical Engineering

This dissertation is accepted by the Graduate School

Lawrence Martin
Dean of the Graduate School

Abstract of the Dissertation

Development of Type-I GaSb-based Diode Lasers and Arrays Operating within Spectral Range above 2µm

by

Jianfeng Chen

Doctor of Philosophy

in

Electrical Engineering

Stony Brook University

2011

This work deals with GaSb-based diode lasers grown by solid source molecular beam epitaxy and operating in high power continuous wave regime at room temperature in mid-infrared spectral region near and above 2 µm.

Firstly, we present experimental and theoretical studies of the effect of the compressive strain above 1% on differential gain and threshold current of GaSb-based type-I quantum well diode lasers on the example of 2.3 µm emitters. The experimental results supported by theoretical calculations conclusively demonstrated that improvement of the hole confinement was primarily responsible for the observed enhancement of the optical gain and the reduction of the threshold current density in laser structures with heavily strained QWs.

Secondly, we introduce quinary AlGaInAsSb as waveguide/barrier material to improve hole confinement in 2.7 μm emitters. Room temperature continuous wave output power of 600 mW was demonstrated for emitters with 470-nm-wide AlGaInAsSb waveguide optimized for improved device differential gain.

Thirdly we describe the design approach and demonstrate the experimental results for 2 μm emitting high power devices with reduced fast axis beam divergence in far field. When asymmetric cladding and non-broadened waveguide design were employed, the fast axis far field beam divergence was reduced from 62° to 37° while keeping favorable threshold current density and internal efficiency.

Finally, we fabricate and characterize single spatial mode room temperature operated 3.15 μm diode lasers. Ridge waveguide lasers generate 9 mW of continuous wave output power in a diffraction limited beam at 20°C.

Table of Contents

List of Tables……………………………………………..…………………..…viii

List of Figures……………………………………………………………………….ix

Acknowledgments ………….……………………………………………………..xiv

Publications………………………………………………………………………...xv

I. Type I GaSb-based Laser Heterostructure Design…………...……………………1

II. Carrier Confinement in QWs with Compressive Strain Above 1%

2.1 Introduction…………………………..……………………………………….11

2.2 Sample Preparation…………………………………………………………..13

2.3 Experiment…………………………………………………………………...16

2.4 Modeling……………………………………………………………………..21

2.5 Discussion……………………………………………………………………27

2.6 Summary……………………………………………………………………..29

2.7 Appendix……………………………………………………………………..30

III. Carrier Confinement in QWs with Quinary AlInGaAsSb as Waveguid Material

3.1 Introduction…………………………………………………………………..38

3.2 Heterostructure………………………………………………………………39

3.3 Experiment.…………………………………………………………………..41

3.4 Summary……………………………………………………………………..43

3.5 Appendix……………………………………………………………..44

IV. Beam Properties

4.1 High Power 2 μm Diode Lasers with Asymmetric Waveguide

4.1.1 Introduction…………………………………………………….…..52

4.1.2 Diode laser fabrication and preliminary characterization….……....56

4.1.3 Experimental studies of the laser gain and loss……………………60

4.1.4 Room temperature CW operation…………………………….……65

4.1.5 Summary……………………………………….……………..69

4.2 1.95 μm Diode Lasers with Asymmetric Waveguide and Improved Properties

4.2.1 Introduction…………………………………………………….…..71

4.2.2 Laser heterostructures……………………………………….…..71

4.2.3 Experiment…………………………………………….……….…..73

4.2.4 Summary…………………………………………………….…..76

4.3 Appendix…………………………………………………………..…77

V. Single Spatial Mode

5.1 Introduction……………………………………………………………..83

5.2 Laser heterostructure…………………….……………………………...84

5.3 Gain guided multimode lasers……………….………………………...94

5.4 Single spatial mode ridge lasers…………….………………………….....86

5.5 Conclusion………….……………………………...................................89

5.6 Appendix……….………………………………….......................................90

References……………………………………………………………………91

List of Tables

Tables **Page**

4.1 Composition and width of the claddings and core layers of the 2 μm emitting laser heterostructures studied. ……………………………………………………...….57

List of Figures

Figures **Page**

1.1 Schematic energy band diagram of GaSb-based type-I laser heterostructure..2

2.1 Schematic energy-band diagram of the broadened waveguide 2.3 μm wavelength In(Al)GaAsSb/GaSb diode lasers…………………………….....…13

2.2 Schematic of the experimental setup used for the pulse anodic oxidation (anodiazation) ……………………………………………………………15

2.3 Tailing edge current in the pulse anodization……………………………..……15

2.4 Pulsed (200 ns / 1 MHz) light-current characteristics of 1-mm-long uncoated lasers with 1 % and 1.5 % of compressive strain in InGaAsSb QWs. Inset shows room temperature laser spectra near threshold …………………………..…...……17

2.5 Temperature dependences of the laser threshold current for moderately and heavily strained lasers……………………………………….…………………..…..17

2.6 Current dependences of the gain spectra measured at 293 K for (a) moderately strained and (b) heavily strained lasers……………………...…………………...19

2.7 Current dependences of the peak modal gain measured for moderately and heavily strained devices at 200 K and 293 K…………………………….....……..20

2.8 Isostrain lines in quaternary GaInAsSb alloy system: dash-doted lines – alloy composition lattice matched to GaSb, dashed lines composition with 1.0 % compressive strain, solid lines - 1.5 % compressive strain. (a) Arsenic vs. indium

concentration in InGaAsSb alloys. (b) Fundamental energy gap in InGaAsSb alloys with different strains. (c) Strain-induced modification of the heavy-hole band edge position……………………………..……………………….……...22

2.9 Strain-induced balancing of electron and hole DOS: (a) Lattice matched $Al_{0.5}Ga_{0.5}As_{0.04}Sb_{0.96}/Ga_{0.8}In_{0.2}As_{0.2}Sb_{0.8}$ QW heterostructure; (b) Strained $Al_{0.25}Ga_{0.75}As_{0.02}Sb_{0.98}/Ga_{0.65}In_{0.35}As_{0.09}Sb_{0.91}$ QW heterostructure with compressively strained QW (strain 1.5 %)……………………………….......24

2.10 Valence band profiles for structures with 1 % compressive strain (dashed line) and 1.5 % strain (solid line): (a) valence band edge position for QWs without injected carriers; (b) self-consistent QW profile for QW carrier concentration $2x10^{12}$ cm^{-2}………………………………......………………………..…25

2.11 Peak modal gain as a function of the injected carrier concentration in QW for different temperatures...……………………………………………………26

3.1 CW light-current and power-conversion characteristics of 2.7 µm emitting 2-mm-long AR/HR coated lasers…………………………………………..…40

3.2 Current dependences of the modal gain spectra measured at 20°C for 1-mm-long uncoated devices. The inset shows the corresponding dependence of the peak modal gain on current………………………………………..……42

3.3 Pulsed light-current characteristics of 2.7 µm emitting 2-mm-long AR/HR coated lasers. The inset shows the fast axis far field divergence measured in CW regime……………………………………..…………………………43

4.1.1 Calculated band alignment diagram and transverse near field distribution of (a) symmetric broadened waveguide laser structure 1 and (b) asymmetric narrow waveguide laser structure…………………..…………………..…………….58

4.1.2 Dependences of the threshold current at 20 ^{0}C (solid circles) and parameter T_0 (open circles) on waveguide core thickness (lines are guide for eye only). Measurements were performed under pulsed excitation (200ns/100kHz) for 1-mm-long, 100-μm-wide uncoated lasers mounted epi-side up onto gold coated copper blocks………………………………………………………….…………59

4.1.3 Measured fast axis far field distributions of 2 μm emitting laser diodes with 1-mm-long, 100-μm-wide uncoated cavities. Structure numbers correspond to table 4.1...……………………………………………………………………..60

4.1.4 Modal gain spectra measured at several under threshold currents for 1-mm-long, 100-μm-wide uncoated lasers. Structure numbers correspond to table 4.1…………..……61

4.1.5 Current dependences of the peak modal gain measured for lasers with structures 1, 3, 4 and 5 (Table 4.1) ....………………………………………62

4.1.6 CW power and power conversion characteristics measured at 20°C for 1- and 2-mm-long, AR/HR coated lasers with structure 3..........……………….……65

4.1.7 CW power and power conversion characteristics measured at 20^{0}C for 2-mm-long, AR/HR coated 18-element linear laser array with structure 3. The array fill- factor was 20%, i.e. 100-μm-wide emitters with 500-μm pitch. The inset shows the corresponding near field....…………...………………………………66

4.1.8 CW power and power conversion characteristics measured at 20^{0}C for 1- and 2-mm-long, AR/HR coated lasers with structure 4. Inset shows laser spectrum……..….67

4.1.9 Fiber coupled CW power generated by seven 2-mm-long AR/HR coated devices with structure 4. The inset shows the near field image of the fiber bundle output……...68

4.1.10 CW power and power conversion characteristics measured at 20^{0}C for 1- and 2-mm-long, AR/HR coated lasers with structure 6. Inset shows laser spectrum…………………………………………………………………….69

4.2.1 (a) Calculated band diagram of the laser heterostructure overlapped with near field distribution; (b) corresponding far field patterns measured in slow and fast axis directions.……………………………….……………...………….72

4.2.2 cw power and power conversion characteristics of 100 μm wide 3 mm long AR/HR coated devices measured at 20 ℃…………………………………....74

4.2.3 Modal gain spectra measured 200 ns/1 MHz at several currents below threshold for 1 mm long uncoated lasers. Inset shows the current dependences of peak modal gain..…………………………………………………………...75

5.1 Temperature dependence of short pulse (200 ns, 10 kHz) light-current characteristics for 1 mm-long, 100 mm-wide, uncoated lasers…..............……...85

5.2 SEM image of front facet section of ridge waveguide laser, and ridge waveguide laser spectra measured in pulsed regime at different heatsink temperatures (top) and in CW regime at 12°C on heatsink. Spectra measured under different conditions shifted vertically for clarity…………………………………………………………...87

5.3 CW light-current-voltage characteristics measured for 12 μm-wide 2 mm-long ridge waveguide lasers in temperature range 15°C – 40°C..89

Acknowledgements

It's difficult to overstate my gratitude to my Ph.D. supervisor Professor Leon Shterengas**.** I appreciate all his encouragement, invaluable suggestions and financial support. In every sense, none of this work would have been possible without his contribution.

I would like to thank the support and guidance of Professor Gregory Belenky. My sincere thanks also go to Prof. Dmitry Donesky, Dr. Sergey Suchalkin and Dr. Gela Kipshidze.

Futhermore I am deeply indebted to my colleagues: Takashi Hosoda, Seungyong Jung and Ding Wang.

Publications

1. R. Liang, **J. Chen**, G. Kipshidze, D. Westerfeld, L. Shterengas, G. Belenky, “High Power 2.2 μm Diode Lasers With Heavily Strained Active Region”, IEEE Photon. Technol. Lett. (Accepted)
2. T. Hosoda, **J. Chen**, G. Tsvid, D. Westerfeld, R. Liang, G. Kipshidze, L. Shterengas, and G. Belenky, “Progress in Development of Room Temperature CW GaSb Based Diode Lasers for 2-3.5 μm Spectral Region”, International Journal of High Speed Electronics and Systems 20, pp. 43-49(2011)
3. G. Tsvid, T. Hosoda, **J. Chen**, G. Kipshidze, L. Shterengas, C. Frez, A. Soibel, S. Forouhr, G. Belenky, “Type-I GaSb Based Single Lateral Mode Diode Lasers Operating at Room Temperature in 3.1-3.2 μm Spectral Region”, Novel In-Plane Semiconductor Lasers X, Photonics West, Proceedings Vol. 7953 (2011)
4. S. Forouhar, C. Frez, A. Ksendzov, Y. Qiu, K. J. Franz, A. Soibel, **J. Chen**, T. Hosoda, G. Kipshidze, L. Shterengas, G. Belenky, “Low power consumption lasers for next generation miniature optical spectrometers for trace gas analysis”, Quantum Sensing and Nanophotonic Devices VIII, Photonics West, Proceedings Vol. 7945 (2011)

5. **J. Chen**, G. Kipshidze, and L. Shterengas, “High Power 2 μm Diode Lasers with Asymmetric Waveguide”, IEEE J. of Quantum. Electron. 46, pp.1464-1469 (2010)

6. **J. Chen**, T. Hosoda, G. Tsvid, R. Liang, D. Westerfeld, G. Kipshidze, L. Shterengas, and G. Belenky, “Type-I GaSb Based Diode Lasers Operating at Room Temperature in 2 to 3.5 μm spectral region”, Proc. SPIE 7686, 76860S (2010)

7. **J. Chen**, G. Kipshidze, and L. Shterengas, “Diode lasers with asymmetric waveguide and improved beam properties”, Appl. Phy. Lett. 96, 241111 (2010)

8. **J. Chen**, T. Hosoda, G. Kipshidze, L. Shterengas, G. Belenky, A. Soibel, C. Frez, and S. Forouhar, “Single Spatial Mode Room Temperature Operated 3.15 μm Diode Lasers”, Electron. Lett. 46, pp. 367-368 (2010)

9. **J. Chen**, G. Kipshidze, L. Shterengas, T. Hosoda, Y. Wang, D. Donetsky, and G. Belenky, “2.7-μm GaSb-Based Diode Lasers With Quinary Waveguide”, IEEE Photon. Technol. Lett. 16, pp. 1112-1114 (2009)

10. L. Shterengas, G. Kipshidze, T. Hosoda, **J. Chen** and G. Belenky, “Diode Lasers Emitting at 3 μm with 300 mW of Continuous-Wave Output Power”, Electron. Lett. 45, pp. 942-943 (2009)

11. **J. Chen**, D. Donetsky, L. Shterengas, M.V. Kisin, G. Kipshidze, and G. Belenky, “Effect of Quantum Well Compressive Strain Above 1% On

Differential Gain and Threshold Current Density in Type-I GaSb-Based Diode Lasers", IEEE J. of Quantum. Electron. 44, pp.1204-1210 (2008)

12. G. Belenky, D. Donetski, L. Shterengas, T. Hosoda, **J. Chen**, G. Kipshidze, and M. Kisin, "Interband GaSb-based laser diodes for spectral regions of 2.3-2.4 μm and 3-3.1 μm with improved room-temperature performance", SPIE, 6900, Quantum Sensing and Nanophotonic Devices V, 690004 (2008)
13. D. Donetsky, **J. Chen**, L. Shterengas, G. Kipshidze, and D. Westerfeld, "2.3 μm High-Power Type I Quantum-Well GaInAsSb/AlGaAsSb/GaSb Laser Diode Arrays with Increased Fill Factor", J. of Electron. Mater. 37, pp. 1770-1773 (2008)

I. Type-I GaSb-based Laser Heterostructure Design

The first task of the laser designer is to select the appropriate material system. Significant progress has been achieved in technology of type-I quantum well (QW) GaSb-based diode lasers. Watt class continuous wave (CW) output power levels were obtained from single laser emitters in spectral region from 2.3 to 2.8 μm at room temperature [1-7]. Recently, the devices operating near 3 μm at room temperature with more than 300 mW of CW output power was reported [8]. These achievements indicate that the III-V compound semiconductor material system (AlGaIn)(AsSb) constitutes a promising basis for the realization of diode lasers in the wavelength regime above 2.0 μm. GaInAsSb, either lattice matched to GaSb or deliberately strained, can be used for the active layer with a direct band gap between 1.7 μm and well above 3 μm. For the barrier and cladding layers, AlGaAsSb is well suited because of its larger band gap energy and lower refractive index than GaInAsSb.

The energy band diagram of type-I GaSb-based semiconductor laser heterostructure is schematically shown in Figure 1.1. Both electrons and holes, injected into the QWs, where they are localized due to the QWs-waveguide energy band discontinuities, will recombine either radiatively or nonradiatively.

The recombination rate can be written as:

$$R_{rec} = R_{nr} + R_r \quad (1.1)$$

where R_{rec} is the total rate of recombination electrons per unit volume in the active region, R_{nr} is the rate of nonradiative recombination, and R_r is the rate of radiative recombination. R_{nr} and R_r can be written as

$$R_{nr} = R_{SRH} + R_{Auger} = AN + CN^3 \quad (1.2)$$

$$R_r = BN^2 \quad (1.3)$$

where R_{SHR} is the Schockley-Read-Hall (SRH) recombination rate, R_{Auger} the Auger recombination rate, N the carrier density in the QWs (quasi-neutrality and absence of background doping is assumed for simplicity), A the nonradiative SRH coefficient, B the radiative coefficient and C the Auger coefficient. This coefficient become concentration dependent when electrons become degenerate under pumping levels required for lasing.

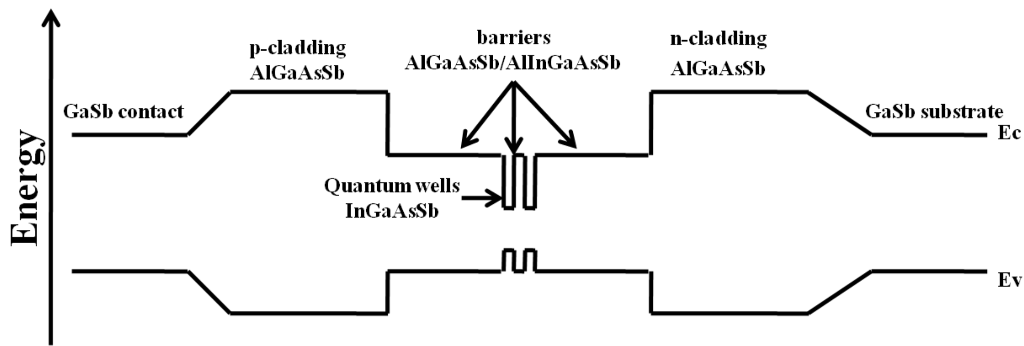

Figure 1.1 schematic energy band diagram of GaSb-based type-I laser heterostructure

The radiation induced photon can interact with valence electrons and be absorbed or can interact with electrons in the conduction band and stimulate an identical photon. When the injected carrier concentration becomes large enough, the stimulated emission can exceed the absorption so that optical gain occurs. The refractive index difference between waveguide and cladding layers helps to localize the optical field mainly within nominally undoped waveguide layer. Due to difference in spatial extends of charge carrier wave function and electromagnetic field mode, the modal gain is given by product of confinement factor (Γ) and material gain (G) which can be written as:

$$G = (I - I_{tr})dg/dI \quad (1.4)$$

Where dg / dI is the differential gain, I the below threshold input current, I_{tr} the transparency current. The expression (1.4) is simplified linearized version of widely used logarithmic dependence of the material gain on current [need reference].

For lasing, it is necessary to arrange for positive feedback. This feedback is often provided by a pair of cleaved facets which are perpendicular to the waveguide axis. The outcoupling loss are often replaced by so called distributed mirror loss that scale with inverse cavity length. Optical wave will also experience the internal loss which is often caused by free carrier intra- and/or inter-band absorption. In the case of intra-band absorption, the photon is absorbed by a free electron or hole, which is excited to a higher energy state in the

conduction or valence band respectively. Due to momentum conservation, this intra-band transition can only take place with the help of an additional interaction with a phonon or an impurity. This mechanism induced optical loss increases in strength with increasing wavelength proportional to λ^k with k in the range of 2 to 3.5. In the case of interband absorption, the absorbed photon energy excites an electron from a filled state in a lower lying band to an empty state in a higher lying band. Total internal loss is comprised of the active layer loss α_a, the waveguide core loss α_{wg}, and the cladding loss α_{cl}(the latter including mode leakage loss, if any):

$$\alpha_{int} = \alpha_a + \alpha_{wg} + \alpha_{cl} \quad (1.5)$$

In GaSb-based diode lasers, the internal loss mainly originates from optical loss in the cladding layers, especially the heavily doped p-cladding layer due to free carrier intervalence band absorption.

After the transparency condition, corresponding pumping of the active region, i.e. injection of the charge carriers from claddings into QWs must create population inversion in QWs. Population inversion condition is defined as:

$$f_c - f_v > 0 \quad (1.6)$$

where f_c and f_v are Fermi distribution functions of electrons in conduction band and holes in valence band. Equation 1.6 implies that the separation of quasi-Fermi levels of electrons and holes must exceed bandgap of the QW material to reach the transparency condition. After the transparency condiction is satisfied, more

current is needed to separate the quasi-Fermi levels of electrons and holes further away to reach the threshold condition. The material gain at threshold G_{th}.:

$$\Gamma \cdot G_{th} - \alpha = 0 \quad (1.7)$$

where

$$\alpha = \alpha_{int} + \alpha_m \quad (1.8)$$

$$\alpha_m = \frac{1}{2L} \ln \left(\frac{1}{R_1 R_2}\right) \quad (1.9)$$

The threshold current I_{th} can be written as:

$$I_{th} = I_{tr} + \frac{\alpha}{dg/dI} \quad (1.10)$$

After threshold condition is reached, the carrier concentration and material gain inside the QWs are pinned at their threshold value which results into that all the extra injected carriers will recombine radiatively due to intensive stimulated emission. Internal efficiency η_{int} characterizes percentage of injected carriers that reach active QWs. Input of electric power will be converted to the output optical power according to:

$$P = \eta_{slope} \cdot (I - I_{th}) \quad (1.11)$$

where η_{slope}-the slope efficiency measured in W/A and defined as:

$$\eta_{slope} = \frac{h\upsilon}{q} \eta_{int} \frac{\alpha_m}{\alpha_m + \alpha_{int}} \quad (1.12)$$

where q-electron charge and $h\upsilon$-photon energy.

Parameters of semiconductor lasers are dependent on temperature since population of the electrons states coupled into the laser mode is governed by

Fermi statistics. In laser engineering changes of the laser threshold and efficiency with temperature are characterized by two parameters: T_0 and T_1.

$$I_{th}(T) = I_{th}(T_{ref}) \cdot \exp\left(\frac{T-T_{ref}}{T_0}\right) \quad (1.13)$$

$$\eta(T) = \eta(T_{ref}) \cdot \exp\left(-\frac{T-T_{ref}}{T_1}\right) \quad (1.14)$$

T_{ref} is certain reference temperature and T is the device temperature. Since contribution of different mechanisms to device thermal sensitivity varies with temperature, T_0 and T_1 are functions of temperature itself. Despite of the lack of physical sense, this T_0 and T_1 terminology is rather convenient and commonly accepted. High values of T_0 and T_1 imply relatively low temperature sensitivity of the device threshold current and slope efficiency and thus desirable. It is important to understand, though, that if two devices have the same rate of increase of the threshold with temperature ($dI_{th}(T)/dT$) but one of them has larger value of $I_{th}(T_{ref})$ at T_{ref}, this high threshold laser will also have higher T_0. Also, T_0 parameter is dependent on T_1 since internal efficiency affects measured value of threshold current.

For the active layers, $Ga_{1-x}In_xAs_y Sb_{1-y}$ is used which has a direct bandgap for all alloy composition and is lattice matched to GaSb if the condition y=0.913x is satisfied. Using a quaternary material for the active layer adds an additional degree of freedom for the design of QWs compared to a ternary material: by changing the composition, two of the three relevant parameters band

gap E_g, strain ε_{zz}, and band offsets ΔE can be adjusted individually within certain limitations. Due to a strong asymmetry between the light conduction band mass and the heavy valence band mass the upper laser levels in the conduction band are almost completely filled with electrons but the lower lasing levels in the valence band are not totally empty. Due to the heavy valence band mass, the holes quasi-Fermi level is above the top of the valence band. Therefore, the holes occupation probability at the top of the valence band is relatively small as compared to the electrons occupation probability at the bottom of the conduction band.

GaInAsSb/AlGaAsSb heterostructures are characterized by strong misbalance between conduction and valence band offsets, i.e. the conduction band offset usually exceeds the one in the valence band. Hence, in spite of large difference between band gaps of AlGaAsSb barrier and GaInAsSb QW materials the holes might be poorly localized while the electrons confinement is more than adequate. There are experimental justifications that type-I QW GaSb-based laser heterostructures suffer from insufficient hole confinement in the QWs [9-10]. Thermionic emission of holes from QWs into, and subsequent recombination within, the barriers is responsible for the decrease of the laser internal efficiency with temperature. Since hole leakage from the QWs is greater in longer wavelength lasers where higher Indium concentration is required in InGaAsSb QWs and thus valence band offset is further reduced, these devices exhibit a greater deterioration in performance with increasing temperature.

Strained layer structures consist of very thin layers where the lattice mismatch is accompanied by a uniform elastic strain that reduces the cubic symmetry of the semiconductors and modifies the electronic and optical properties of the quantum well [11]. The tetragonal distortion raises the degeneracy of the light- and heavy-hole states at the valence band (VB) maximum and makes the effective mass anisotropic with respect to strain direction. The removed degeneracy reduces the density of states at the valence band edge.

Compressive strain can be achieved by decreasing the As composition to make y<0.913x in $Ga_{1-x}In_xAs_y Sb_{1-y}$ QWs and shifts the heavy-hole state upwards. Besides the resulting lower effective mass at the valence band edge, the compressive strain has an additional advantage of increased valence band offset between QWs and barriers. The onset of relaxation in the epitaxial layers should be carefully avoided when strain in the QWs is increased with given layer thickness.

Increasing Aluminum composition in the AlGaAsSb barrier and waveguide layers can also increase the valence band offset between QWs and barriers. To prevent from possible lattice mismatch, As composition also needs to be increased. Associated undesirable effect is unequal distribution of increased energy band gap between conduction and valence band. The more favored increase of conduction band offset will possibly cause inhomogeneous electron distribution in multiple-QW stack. One option to address the strong misbalance between conduction and

valence band offsets is to introduce quinary AlInGaAsSb as barrier and waveguide material which offers the possibility to adjust independently conduction and valence band energy. This independent adjustment would enable us to increase the valence band offset without changing conduction band offset between QWs and barriers.

GaSb-based diode lasers can suffer from a relatively large fast axis far field beam divergence with a full-width at half-maximum (FWHM) of typically 61°-67° [8-10] for state-of-the-art GaSb-based above 2 µm lasers, due to the broadened waveguide design employed. Broadened waveguide design approach is effective in reduction of the optical coupling to doped p-cladding layers and thus improves laser efficieny. However, for practical use of a diode laser in an optical system, the output of the laser has to be collected by optics with a given limited acceptance angle. For a diode laser coupled into an optical fiber, which is the case for most of today's applications, a practical figure of merit is the electrical-to-optical power conversion efficiency with the optical power measured at the end of the optical fiber. Therefore, it is preferred to have a relatively small fast axis beam divergence in far field .

Narrowed far field beam divergence can be achieved by further increasing waveguide core thickness. The associated carrier transport issues might deteriorate the laser internal efficiency. The alternative is to narrow the waveguide core. This will broaden optical near field distribution into cladding

layers and therefore reduce the far field beam divergence in the fast axis. Along with reduced waveguide core thickness, optical field will be equally broadened into heavily doped p-cladding layer where free carrier absorption leads to optical loss. To avoid increased optical field overlap with p-cladding layer, asymmetric waveguide design with reduced refractive index step between waveguide core and n-cladding layer can be employed to introduce the selective penetration of optical field into n-cladding layer where free carrier absorption is substantially less than that in p-cladding layer.

II. Carrier Confinement in QWs with Compressive Strain above 1%

2.1 Introduction

High power room temperature operated GaSb-based diode lasers can serve as a light source for wide range of applications including tunable laser spectroscopy, medical diagnostics and therapy, material processing, as well as infrared illumination and countermeasures. There are experimental justifications that type-I QW GaSb-based laser heterostructures suffer from insufficient hole confinement [12, 13]. Hole confinement can be improved by either adjustment of barrier layer composition [13] or by use of In-rich InGaAsSb QWs with limited arsenic content, i.e. heavily compressively strained QWs. Introduction of compressive strain in active QWs is also known to improve the laser differential gain through reduction of the hole density of states (DOS), i.e. through balancing of the DOS in the joint electron and hole lasing subbands [14]. It is indicated in chapter 1 that presence of nonradiative Auger recombination is not a limiting factor for development of the room temperature operated type-I QW diode lasers for spectral region below 3 μm. However, it is expected that Auger recombination processes should contribute to threshold current density of these mid-infrared

devices so that the design approaches should take special care to minimize such contributions.

We will present detailed experimental and theoretical analysis aimed to identify the role of QW compressive strain in determining mid-infrared type-I QW GaSb-based diode laser threshold current density. For this purpose we have designed and fabricated two laser heterostructures with differently strained QWs characterized by different compositions and, presumably, by different hole confinement energies. Both structures were emitting at 2.3 μm at room temperature and had the same waveguide and contact layer designs. Increase of the QW compressive strain from 1 to 1.5 % led to nearly twofold reduction of the room temperature threshold current density from 230 A/cm^2 down to 120 A/cm^2 for 1mm-long uncoated diode lasers.

Experimental characterization of the lasers included measurements of the laser threshold current density, slope efficiency, optical loss and differential gain with respect to current — all in the temperature range from 100 K to over 300 K. Theoretical calculations were based on the 8-band electron energy spectrum model which included strain-induced modifications of the band positions and Coulomb band bending caused by charge separation due to difference in the electron and hole confinement energies. Experimental and modeling results conclusively demonstrated that improvement of the hole confinement was primarily responsible for the observed enhancement of the optical gain and

twofold reduction of the threshold current density in laser structures with heavily strained QWs. Strain-induced balancing of the subband density of states (DOS) was of secondary importance. It was also noticed that Coulomb attraction of holes to the electrons, strongly localized in QWs, and resulting band bending cannot fully compensate for the lack of valence band discontinuity in GaSb-based laser heterostructures.

2.2 **Sample preparation**

Figure 2.1 schematically depicts the energy bands of the broadened waveguide two-QW 2.3 μm In(Al)GaAsSb/GaSb diode lasers. Laser heterostructures were grown by solid-source molecular beam epitaxy using Veeco

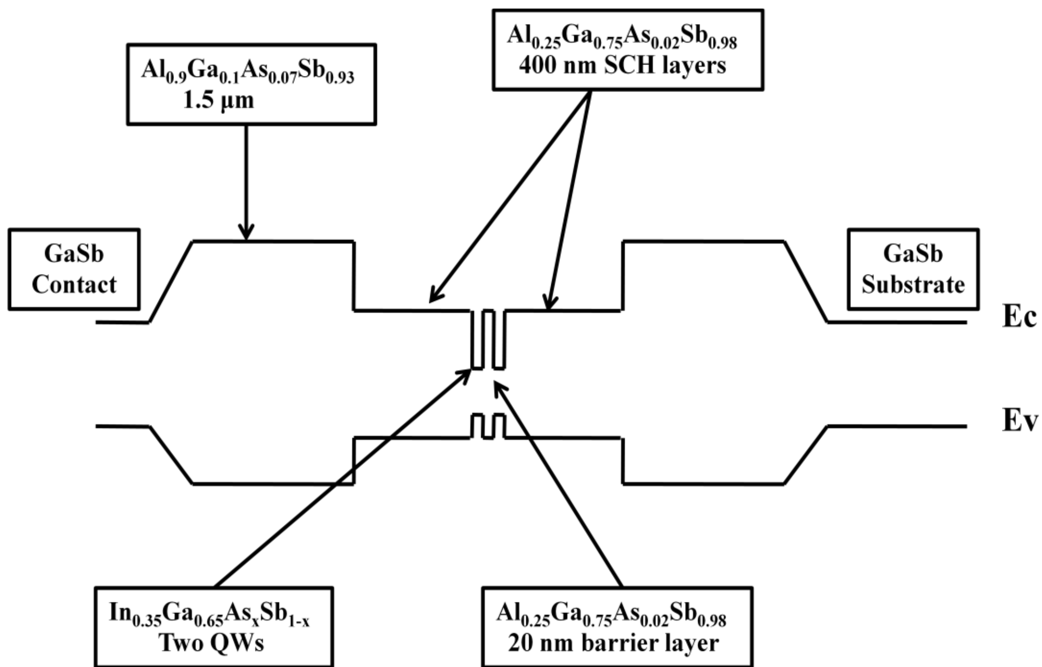

Figure 2.1 Schematic energy-band diagram of the broadened waveguide 2.3 μm wavelength In(Al)GaAsSb/GaSb diode lasers

GEN-930 modular system equipped with valved crackers for both As and Sb. Two heterostructures of identical layer sequence design but with different QW compositions and widths have been grown on n-GaSb substrates doped with Te. The cladding layers were 1.5μm wide $Al_{0.9}Ga_{0.1}As_{0.07}Sb_{0.93}$ doped with Te (n-side) and Be (p-side). Graded bandgap heavily doped transition layers were introduced between the substrate and n-cladding and between the p-cladding and p-cap to assist carrier injection. The nominally undoped $Al_{0.25}Ga_{0.75}As_{0.02}Sb_{0.98}$ waveguide layer with a total thickness of about 800 nm contained two $In_{0.35}Ga_{0.65}As_xSb_{1-x}$ QWs centered in the waveguide and spaced 20 nm apart. The thick waveguide and cladding layers were lattice matched to GaSb. The laser heterostructures used in this work closely corresponded to designs of high power 2.3-2.5 μm diode lasers with above 1W CW output power at room temperature [15-16].

The structure that will be referenced in the text as “moderately strained” one contained 12 nm QWs with compressive strain of 1%. Structure two – “heavily strained” – contained 10 nm QWs with compressive strain of 1.5%. The difference in strain was achieved by changing QW arsenic contents from about 9% (heavily strained) to about 17% (moderately strained). The QW width was reduced from 12 nm to 10 nm for moderately strained structure in order for both lasers to operate at the same wavelength (near 2.3 μm at room temperature).

Both wafers were processed into 100 μm-wide oxide confined gain guided lasers using pulse anodization (PA) technique (figure 2.2) [17-18]. In this

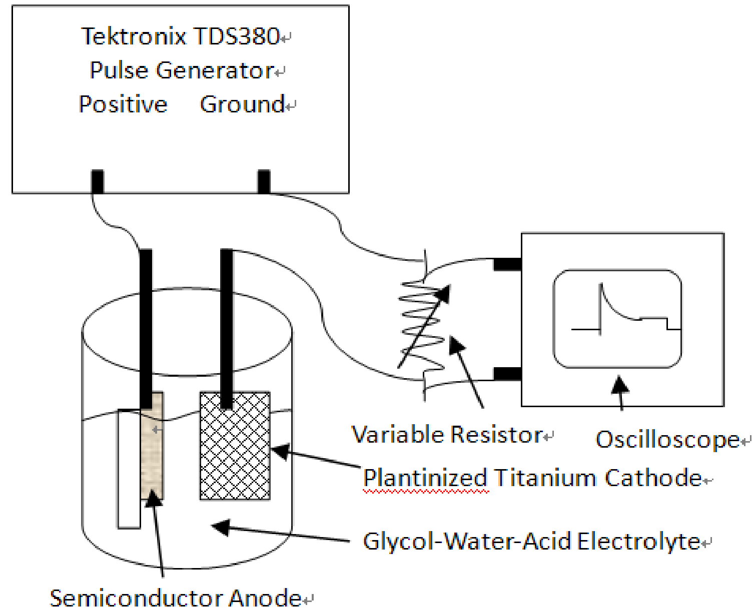

Figure 2.2 Schematic of the experimental setup used for the pulse anodic oxidation (anodiazation)

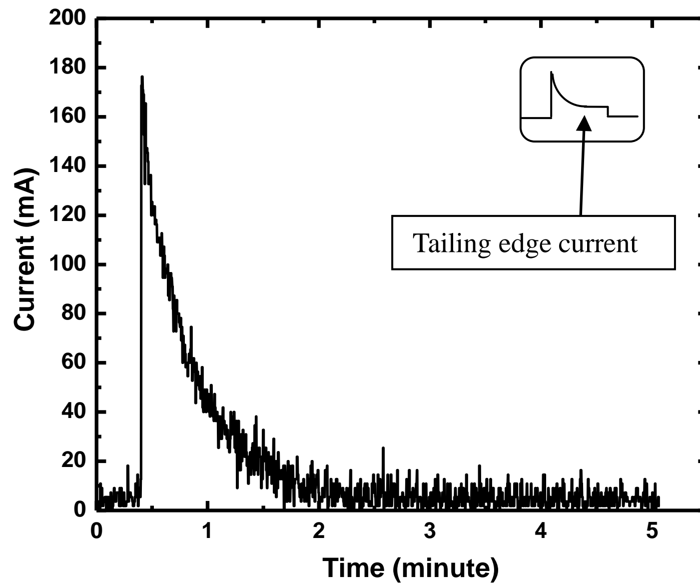

Figure 2.3 Tailing edge current in the pulse anodization

technique native oxide layer was grown in the p-side transition and cladding

layers to define the current stripes. The wafers with photo resist mask were attached to a glass holder with clear wax and put into beaker filled with electrolyte (40 % ethylene glycol, 20 % deionized water and 1 % phosphoric acid). The current pulses (100 mA/cm^2, 700 μs/50 Hz) were sent through the circuit consisting of wafer as an anode, electrolyte bath, platinized titanium as a cathode, and 100 Ohm resistor. Oscilloscope probe connected across 100 Ohm resistor was used to observe temporal development of the current amplitude and the oxidation process was stopped when tailing edge current saturated. The electrolytically grown native oxide was of about 100nm-thick. Standard metallization was applied to p- and n-sides of the wafers. 1mm-long uncoated diode lasers were In-soldered epi-side up onto Au-coated polished copper blocks. The devices have been mounted either onto thermoelectrically cooled copper block or onto cold finger of liquid nitrogen cooled cryostat and characterized in pulsed mode (200 ns/1 MHz).

2.3 Experiment

Figure 2.4 shows the light-current characteristics measured at room temperature (20 ^{0}C) for moderately strained and heavily strained diode lasers. Threshold current density of about 230 A/cm^2 was measured for moderately strained lasers and only 120 A/cm for heavily strained devices. Heavily strained devices also tend to have higher slope efficiency (0.16 W/A per facet) than low strain ones (0.14 W/A per facet).

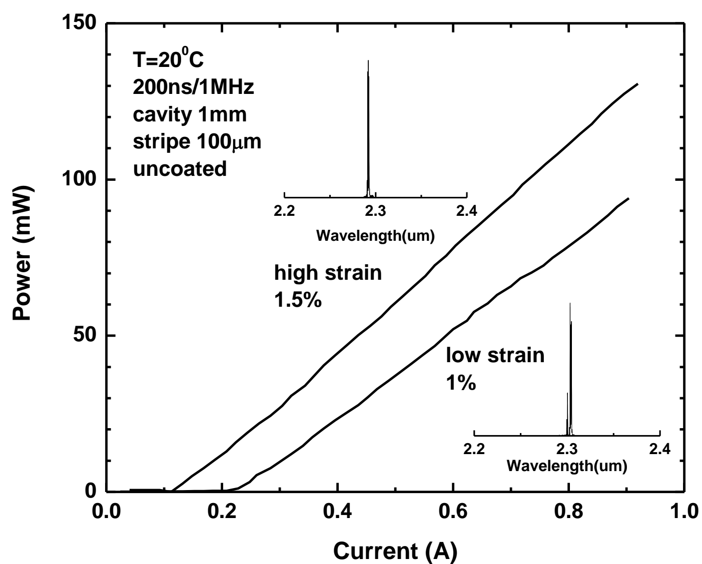

Figure 2.4 Pulsed (200 ns / 1 MHz) light-current characteristics of 1-mm-long uncoated lasers with 1 % and 1.5 % of compressive strain in InGaAsSb QWs. Inset shows room temperature laser spectra near threshold.

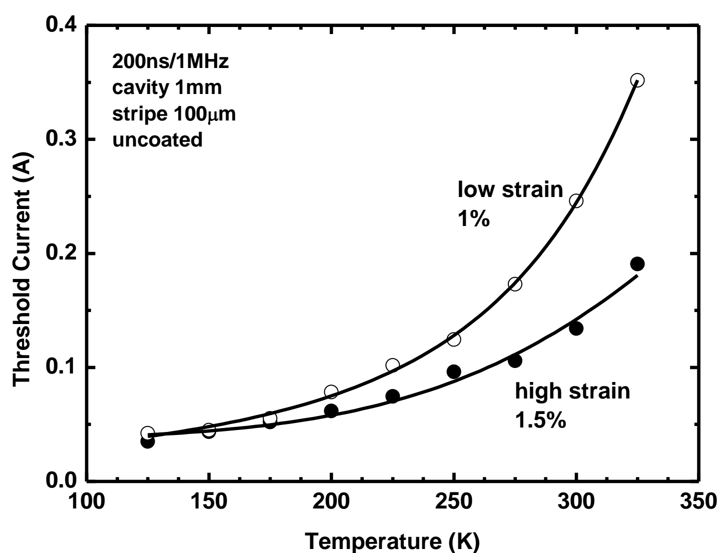

Figure 2.5 Temperature dependences of the laser threshold current for moderately and heavily strained lasers.

At low temperatures (Figure 2.5) the threshold currents for both structures become nearly identical and equal to 40 mA (20 A/cm^2 per QW) at 150 K. At 200 K the threshold current of heavily strained lasers is already slightly larger than that of moderately strained ones and the difference tends to increase with temperature. In room temperature range the moderately strained lasers demonstrate nearly twofold higher threshold currents as compared to heavily strained devices.

In order to identify the reason for the observed dependence of the laser threshold current on active region strain the corresponding laser modal gain spectra have been studied. Figure 2.6 shows the current dependences of the modal gain spectra for 100-μm-wide 1-mm-long uncoated lasers measured at 293 K. Modal gain spectra were obtained using Hakki–Paoli method [19] supplemented by spatial filtering optics to separate only the on-axis mode of the multimode gain guided lasers. Figure 2.6 data allows for estimating several laser parameters, namely, internal optical losses, differential gain with respect to current, and transparency current. Internal optical losses can be determined from the low energy part of the modal gain spectra where the spectra measured at different currents converge to the total modal losses. Modal gain in the low energy limits approaches about 16 cm^{-1} for both types of lasers. By utilizing equation 1.8, the mirror losses are estimated to be 12 cm^{-1} for a 1mm-long as-cleaved lasers leaving a value for internal optical loss of 4 cm^{-1}. Thus, it was confirmed that the

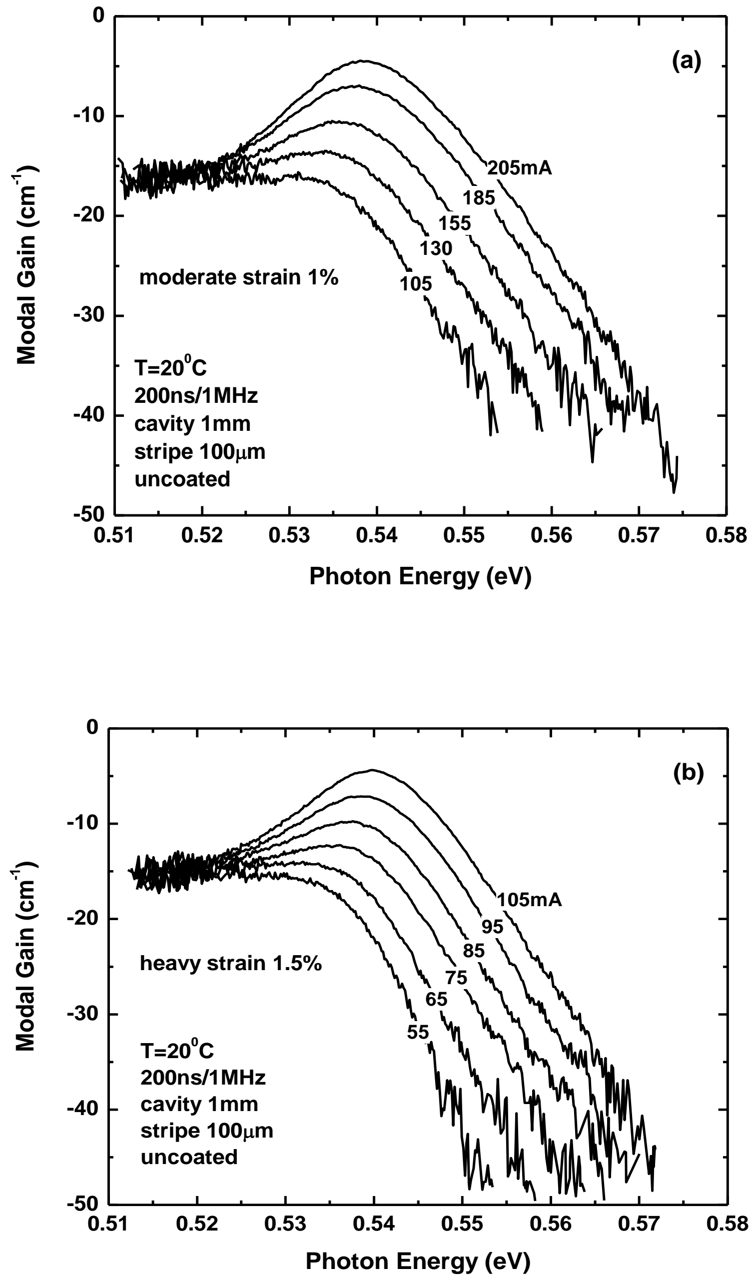

Figure 2.6 Current dependences of the gain spectra measured at 293 K for (a) moderately strained and (b) heavily strained lasers.

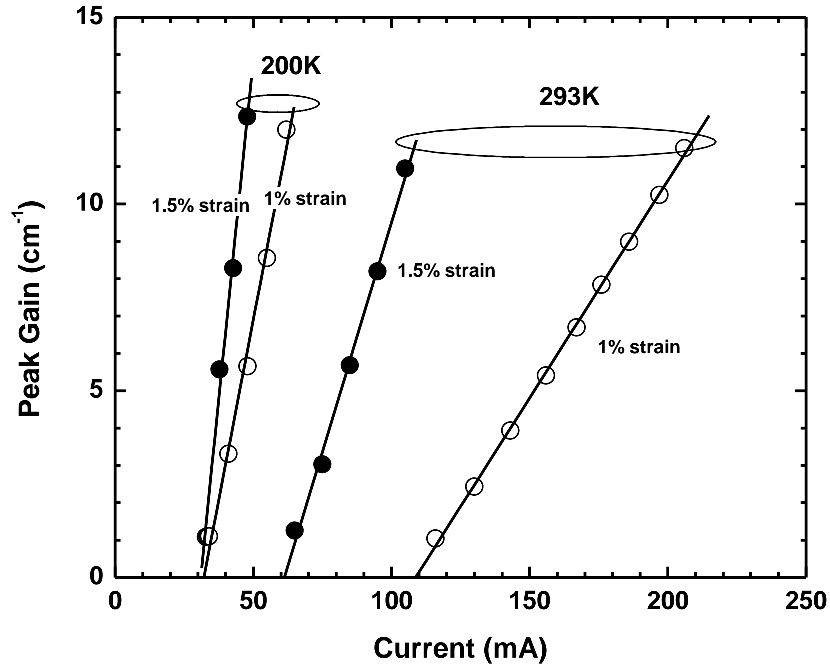

Figure 2.7 Current dependences of the peak modal gain measured for moderately and heavily strained devices at 200 K and 293 K.

internal optical loss value is independent on active region strain and the difference in threshold currents between moderately and heavily strained lasers cannot be attributed to difference in optical losses. Figure 2.7 plots the current dependences of the peak modal gain measured at 200 K and 293 K. Room temperature data (293 K) show strong dependence of the differential gain and transparency current on laser active region strain. Heavily strained devices demonstrated increase of differential gain from 120 cm^{-1}/A up to 250 cm^{-1}/A and reduction of the transparency current from 120 mA down to 60 mA as compared to moderately strained lasers. A twofold difference in the differential gain and transparency

current accounts for a twofold lower room temperature threshold current in the heavily strained devices. At low temperatures the differences in both the differential gain and transparency current between moderately and heavily strained lasers tend to decrease. Figure 2.7 shows that at 200 K the transparency current values for both types of the devices are about 30mA while the differential gain increases up to 730 cm^{-1}/A for heavily strain lasers and up to 390 cm^{-1}/A for moderately strain ones. Despite the difference in differential gains still remains considerable at 200 K (though smaller than at room temperature) the similar values of the transparency currents and high values of the differential gains lead to small relative difference in threshold currents, namely 60 mA for heavily strained and about 80 mA for moderately strain devices. When temperature decreases below 200 K the difference in threshold currents between moderately and heavily strained lasers tends to disappear.

2.4 Modeling

Effect of the QW compressive strain on the laser performance was analyzed by calculating the modal optical gain in moderately (1 %) and heavily (1.5 %) strained laser structures. 8-band Schrödinger equation was solved self-consistently with the Poisson equation using the COMSOL software [20]. During each iteration, the hole populations and Fermi distribution functions in each hole subband were recalculated taking into account thermal redistribution of holes between the QWs and waveguide. The iteration cycle was repeated until quasi-

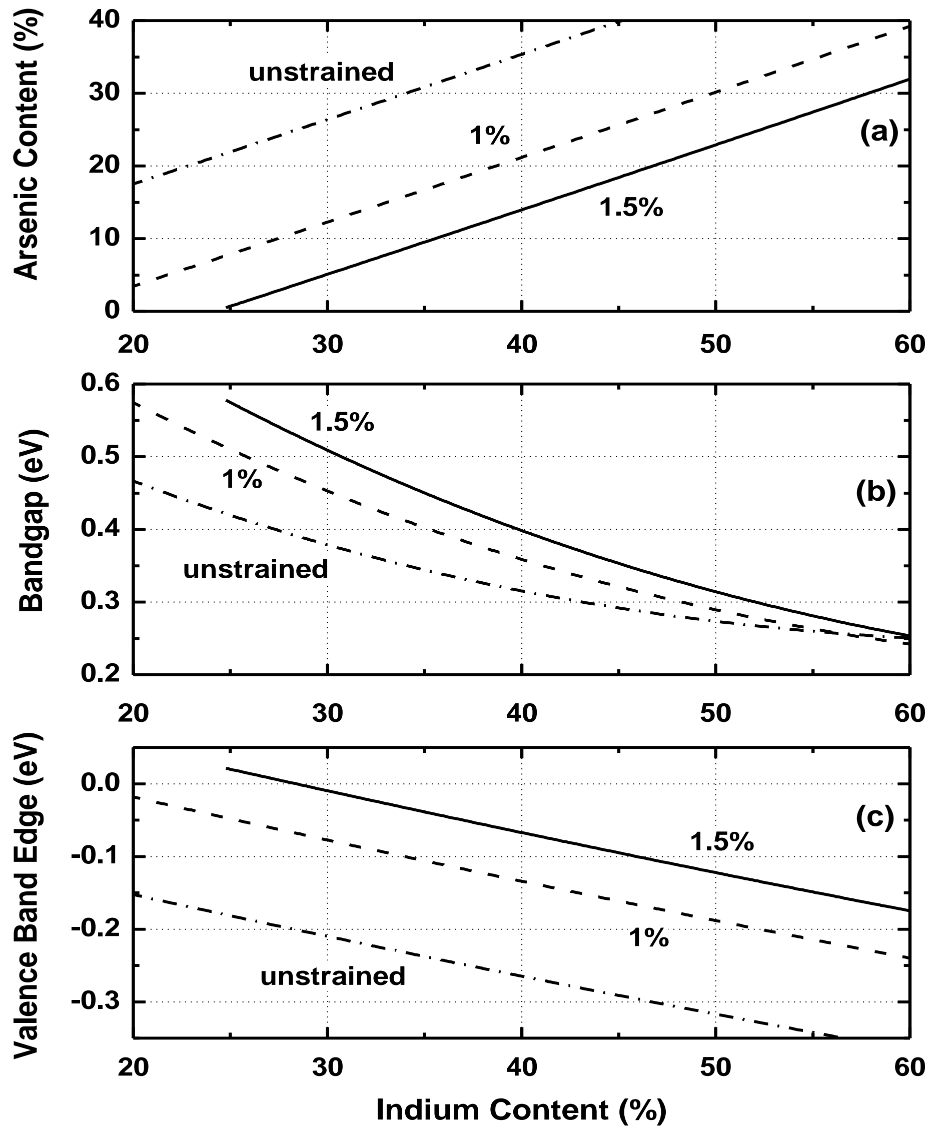

Figure 2.8 Isostrain lines in quaternary GaInAsSb alloy system: dash-doted lines - alloy composition lattice matched to GaSb, dashed lines – composition with 1.0 % compressive strain, solid lines - 1.5 % compressive strain. (a) Arsenic vs. indium concentration in InGaAsSb alloys. (b) Fundamental energy gap in InGaAsSb alloys with different strains. (c) Strain-induced modification of the heavy-hole band edge position. Horizontal dashed line indicates the positions of the valence band edge in the AlGaAsSb barrier with 25 % aluminum concentration.

Fermi level position in valence band has been stabilized and solution conversion reached, which took 5-10 iterations depending on the injected carrier concentration and temperature. Data for binary materials and ternary alloys used in these calculations were taken from review [21]. The quaternary alloy band gaps were calculated using biquadratic interpolation algorithm [22]. Figure 2.8a shows the arsenic vs. indium composition dependencies for iso-strain QW compositions. The compositions with indium contents above 30 % are of major interest for the QW MIR-lasers. Figures 2.8b and 2.8c show the calculated energy gaps and, correspondingly, the heavy-hole band edge positions in quaternary InGaAsSb compositions with different values of the compressive strain. It is readily seen that highly strained indium-rich QW compositions benefit from improved hole confinement while retaining sufficiently low values of the optical gap.

Figure 2.9 illustrates the process of strain-induced balancing of the electron and hole DOS in GaSb-based QW heterostructures. Figure 2.9a shows energy subbands (left panel) and subband DOS (right panel) in an exemplary lattice matched (unstrained) $Al_{0.5}Ga_{0.5}As_{0.04}Sb_{0.96}/Ga_{0.8}In_{0.2}As_{0.2}Sb_{0.8}$ QW structure. Electron and hole subbands have noticeably different DOS in an unstrained QW due to the anticrossing between second (heavy-hole) and third (light-hole) valence subbands, which induces strong subband nonparabolicity. Figure 2.9b demonstrates much better balance between lower electron and upper hole subband DOS in $Al_{0.25}Ga_{0.75}As_{0.02}Sb_{0.98}/In_{0.35}Ga_{0.65}As_{0.09}Sb_{0.91}$ heterostructure (heavily

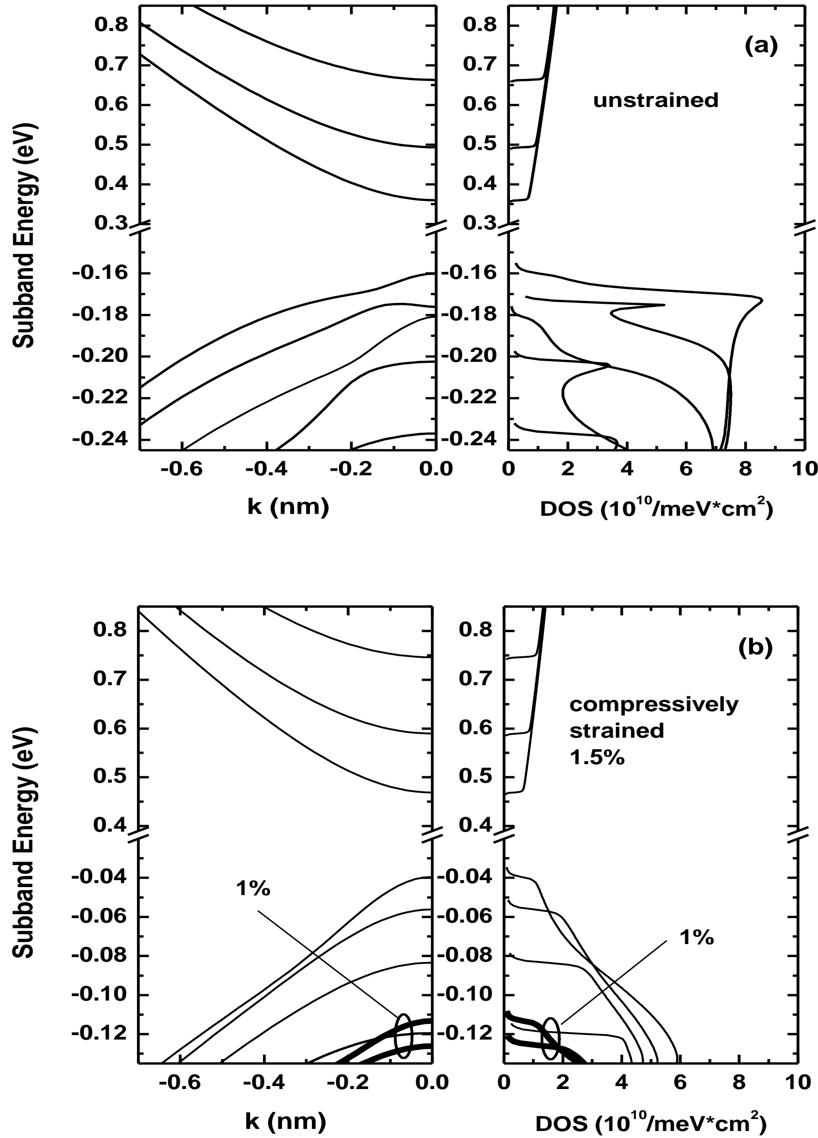

Figure 2.9 Strain-induced balancing of electron and hole DOS: (a) Lattice matched $Al_{0.5}Ga_{0.5}As_{0.04}Sb_{0.96}/Ga_{0.8}In_{0.2}As_{0.2}Sb_{0.8}$ QW heterostructure; (b) Strained $Al_{0.25}Ga_{0.75}As_{0.02}Sb_{0.98}$ $/Ga_{0.65}In_{0.35}As_{0.09}Sb_{0.91}$ QW heterostructure with compressively strained QW (strain 1.5 %). Left panel of each plot shows the subband dispersion, i.e. the subband energy vs. the electron/hole wavevector k; right panel shows the subband DOS (in 10^{10} /meV*cm^2). Note the difference in energy scale for valence band subbands in figures (a) and (b). Two bold lines in the lower part of each panel of figure (b) show valence subbands and DOS for QW composition $Ga_{0.65}In_{0.35}As_{0.17}Sb_{0.83}$ with 1 % strain.

strained laser in section III) with highly compressively strained QW (strain 1.5 %). All three upper hole subbands in this heterostructure are of heavy-hole type at k = 0 and no anticrossing effects are visible in the subband DOS structure. Bold lines in lower part of Figure 2.9b depict the valence subbands and, correspondingly, DOS for a QW with higher arsenic concentration and lower strain (moderately strained structure in section III with arsenic content of 17 % and QW compressive strain of 1 %). It is readily seen that the DOS value at the upper subband edge does not differ noticeably between QWs with 1 % and 1.5 % of compressive.

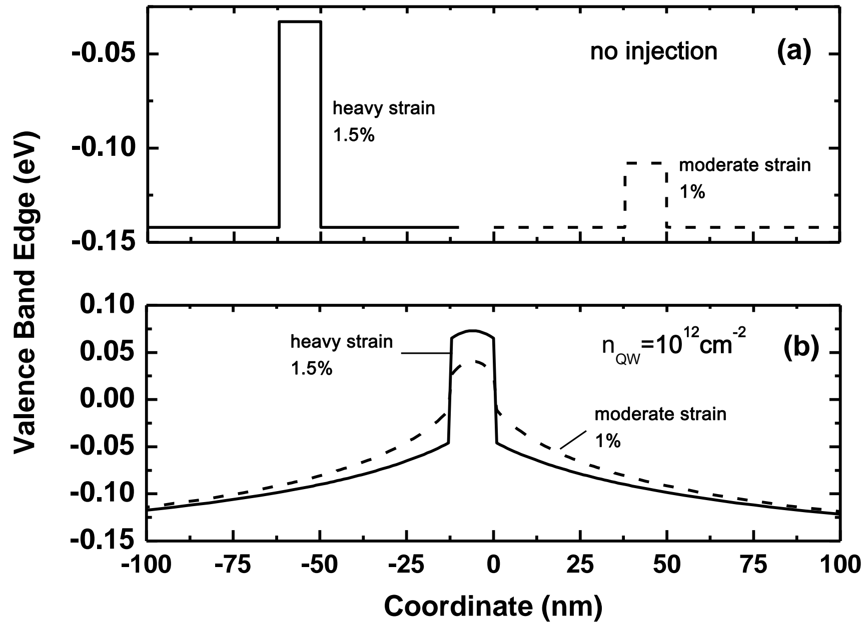

Figure 2.10 Valence band profiles for structures with 1 % compressive strain (dashed line) and 1.5 % strain (solid line): (a) valence band edge position for QWs without injected carriers; (b) self-consistent QW profile for QW carrier concentration $2x10^{12}$ cm^{-2}.

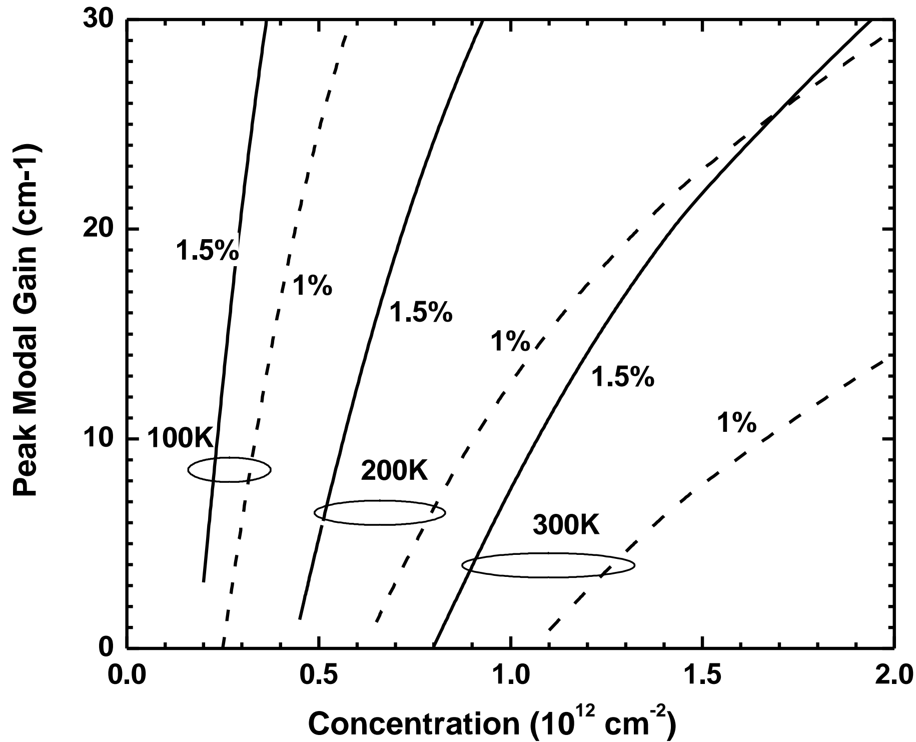

Figure 2.11 Peak modal gain as a function of the injected carrier concentration in QW for different temperatures. Dashed lines indicate structure with 1 % compressive strain (moderate strain), solid lines – structure with 1.5 % strain (heavy strain). waveguide and, for the same total carrier concentration, increases the occupation of the upper heavy-hole subband states participating in the lasing transition.

The QW depth for electrons is more than adequate in both structures so that the electrons predominantly occupy the lowest electronic subband with negligible thermal redistribution into the higher subbands even at room temperature. According to our estimation, QW depths for heavy holes were 35 meV in moderately strained and 105 meV in heavily strained structures (Figure 2.10a). Deficit of the hole confinement in the moderately strained structure in

combination with large value of valence band DOS in bulk waveguide layers leads to strong thermal hole redistribution and reduces the population of the hole lasing states. On the other hand, different spatial distribution of the electrons and holes induces the band bending which to some extent improves the hole confinement in low strain structure (figure 2.10b).

Figure 2.11 shows peak modal gain calculated at 100, 200 and 300 K as a function of the injected carrier concentration for structures with moderate strain (dashed lines) and heavy strain (solid lines). Structure with heavily strained QWs and, hence, better hole confinement demonstrates higher differential gain and lower transparency concentration as compared to moderately strained structures. Strain-induced deepening of the heavy hole QW reduces thermal redistribution of the holes between QW and waveguide and, for the same total carrier concentration, increases the occupation of the upper heavy-hole subband states participating in the lasing transition.

2.5 Discussion

In InGaAsSb/AlGaAsSb quantum wells (QWs) the band offsets at the heterointerfaces are unevenly distributed between conduction and valence bands leading to excessive electron and deficient hole confinements. Since the electrons are strongly localized in deep conduction band QWs, the thermal redistribution of holes between the shallow valence band QWs and the optical waveguide layers creates Coulomb barriers which can improve the hole confinement to some extent.

Even in this case, however, the bulk heavy-hole states of the waveguide material with very high DOS remain energetically close to the lasing states in the uppermost hole subband and, therefore, unfavorably affect the population of the lasing states. This situation can be improved by using the compressively strained QW layers.

Compressive strain splits the first heavy-hole and first light-hole subbands and reduces the band-edge hole DOS, which otherwise is unfavorably increased by heavy-light subband mixing [14]. This mechanism of gain improvement, however, works well only for compressive strain level up to 1 % [23]. Strain values beyond that range have minor effect on the band-edge heavy-hole DOS, since at such a high strain the heavy-hole and light-hole subbands are already well separated in energy. In this work we have demonstrated that, due to the inherently low valence band offsets at the quaternary InGaAsSb/AlGaAsSb interfaces, the QW compressive strain manifests itself not only through the band-edge hole DOS reduction but, mainly, by increasing the effective barrier height for the quantum-confined hole states. Compressive strain moves the position of the QW heavy-hole states upwards thus making the heavy-hole QW deeper. Improved hole confinement, in turn, reduces the thermally activated hole redistribution between the QW subbands and the adjoin bulk barrier states and, therefore, increases the occupation of the uppermost hole subband states participating in the lasing transition. This ultimately enhances the laser differential gain and reduces the

threshold current density. The calculations prove that the enhancement of the optical gain in Sb-based lasers through the strain-induced increase of the heavy-hole confinement remains efficient for high compressive strain in the 1 - 2 % range while preserving the benefit of the balanced joint DOS achieved at the lower strain level.

Reduction of the laser threshold concentration in structures with heavily strained QWs also minimizes the contribution of the Auger processes though cannot eliminate them completely. The carrier concentration required to reach lasing threshold increases with temperature (Figure 8). In moderately strained structures with inadequate valence band offset there is a need for the extra carrier injection that comes from the necessity to occupy a set of closely separated hole subbands with inherently large density of states. Corresponding increase of the threshold carrier concentration triggers Auger processes which in turn increase the laser threshold current density and worsen temperature stability of the device.

2.6 Summary

Experiment demonstrates that the use of the InGaAsSb quantum wells with compressive strain above 1 % is an effective tool for the reduction of the laser threshold current, especially at room temperatures. Calculations show that strain-induced improvement of the hole confinement is primarily responsible for the observed improvement of the laser performance. In contrast to strain-induced DOS balancing, which is efficient for strain values up to 1 %, this mechanism

remains efficient at higher compressive strain levels. GaSb-based diode lasers designed for room temperature operation at 2.3 µm demonstrate twofold reduction of the threshold current density from about 250 A/cm^2 down to 120 A/cm^2 when QW compressive strain is increased from 1 % up to 1.5 %. Measurements of the device differential gain and transparency current show that the observed improvement of the laser threshold is explained by the twofold increase of the differential gain (with respect to current) and transparency current reduction. At lower temperatures, when the hole confinements become adequate in both 1 % and 1.5 % compressively strained QWs, the dependence of the laser threshold current on QW compressive strain tend to disappear.

2.7 Appendix

2.7.1 Fabrication steps:

1. Pulsed anodization

   a. Prepare electrolyte solution (40% ethylene glycol, 20% deionized water and 1% phosphoric acid) and leave it spin for at least 1 day

   b. Sample preparation—HCl:H_2O=1:10 for 60 sec and dry with N_2 blast

   c. Lithography (Photoresist— NR1-3000PY, Developer—RD6)

      i. Spin— 4000 RPM for 40 sec

      ii. First bake—on hotplate at 130°C for 120 sec

      iii. Exposure—10 mW/cm^2 for 33 sec

      iv. Second bake—on hotplate at 110 ℃ for 80 sec

v. Develop—RD6 for 27 sec

d. Pulsed anodization

-Send current pulses (100 mA/cm^2, 700 μs/50 Hz) through the circuit consisting of wafer as an anode, electrolyte bath, platinized titanium as a cathode, and 100 Ohm resistor until tailing edge current saturated.

e. Clean

i. Clean photoresist—rinse with aceton to wash off photoresist

ii. O_2 plasma—160 mW for 60 sec $\times 3$ times

2. P-side metal deposition (Ti/Au) - E-beam metal deposition (Temescal BJD)

a. Wait till the pressure going down below 1.0×10^{-6} Torr

b. Turn on heat, set the chamber temperature at 70 ℃, and wait again for an hour or two

c. Ar plasma for 60 sec (1.0×10^{-4} Torr/Ar ~3 sccm/Beam Voltage 500 V/40 mA)

d. Wait until the chamber temperature cool down to room temperature

e. Deposition

-Ti (200 Å)/ Au (1000 Å)

f. Liftoff— rinse with Aceton to wash off photoresist

g. O_2 plasma—160 mW for 60 sec $\times 3$ times

3. Lapping and polishing

a. Lap down substrate to 100-130 μm (use 3 μm aluminum oxide powder)

b. Polish the surface—use solution of 20 nm TiC (5 ml)/Water (50 ml)/Clorox

(5-10 ml)

4. First n-side metal deposition (Ni/Au/Ge/Ni/Au)

a. Sample preparation—$NH_4OH:H_2O$=1:20 for 20 sec and dry with N_2 blast

b. E-beam metal deposition (Temescal BJD)

i. Wait till the pressure going down below 1.0×10^{-6} Torr

ii. Turn on heat, set the chamber temperature at 120 ℃, and wait again for an hour or two

iii. Ar plasma for 60 sec (1.0×10^{-4} Torr/Ar ~3 sccm/Beam Voltage 500 V/40 mA)

iv. Wait till the chamber temperature cool down to room temperature

v. Deposition

-Ni (50 Å)/Au (450 Å)/Ge (200 Å)/Ni (150 Å)/Au (2000 Å)

c. Rapid Thermal Processing (ramp 30 sec from room temperature to 250 ℃/stay at 250 ℃ for 120 sec)

-n-side metal layer diffuses in semiconductor and looks shiny white (becomes ohmic contact)

5. Second n-side metal deposition (Ti/Au)

a. Sample preparation—N_2 blast (dust off from surface)

b. E-beam metal deposition (Temescal BJD)

i. Wait till the pressure going down below 1.0×10^{-6} Torr

ii. Ar plasma for 60 sec (1.0×10^{-4} Torr/Ar ~3 sccm/Beam Voltage 500 V/40

mA)

iii. Wait till the chamber temperature cool down to room temperature

iv. Deposition

-Ti (200 Å)/Au (1000 Å)

2.7.2 Labview program for pulsed light-current characteristics measurement

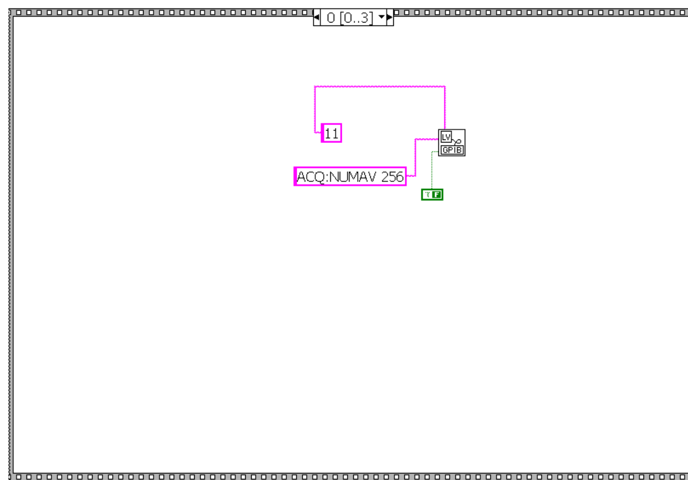

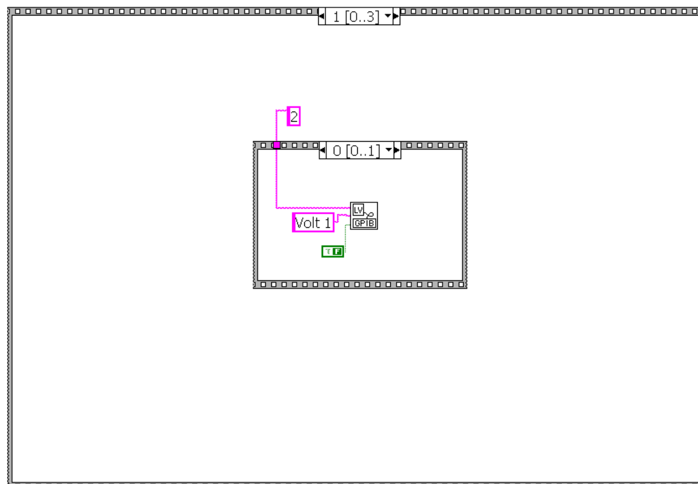

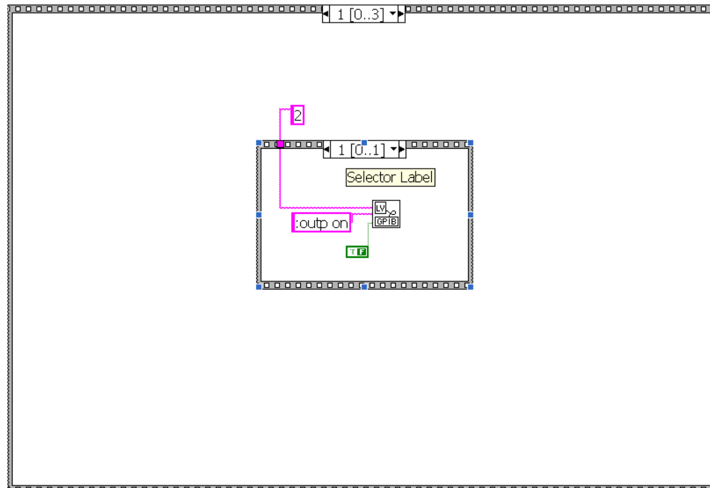
1 [0..3]
2
1 [0..1]
Selector Label
:outp on

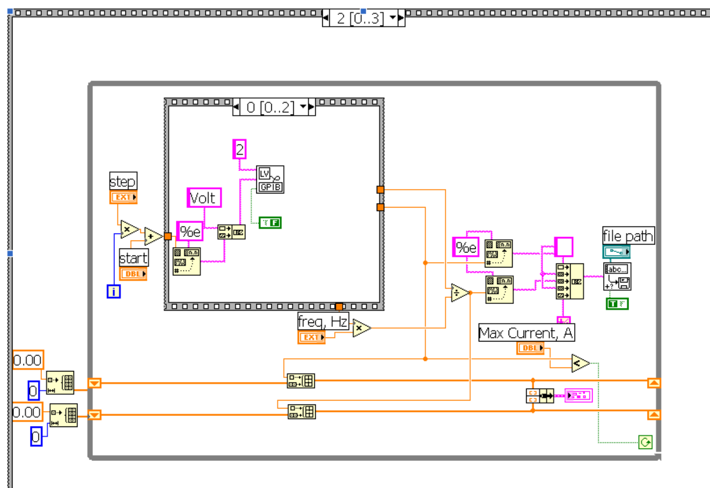
2 [0..3]
0 [0..2]
2
Volt
step
%e
start
file path
Max Current, A
freq, Hz
0.00
0
0.00
0

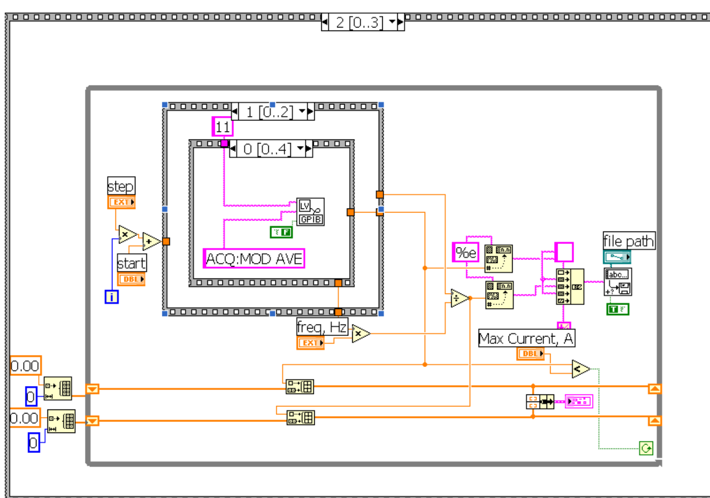
2 [0..3]
1 [0..2]
11
0 [0..4]
step
start
ACQ:MOD AVE
%e
file path
Max Current, A
freq, Hz
0.00
0
0.00
0

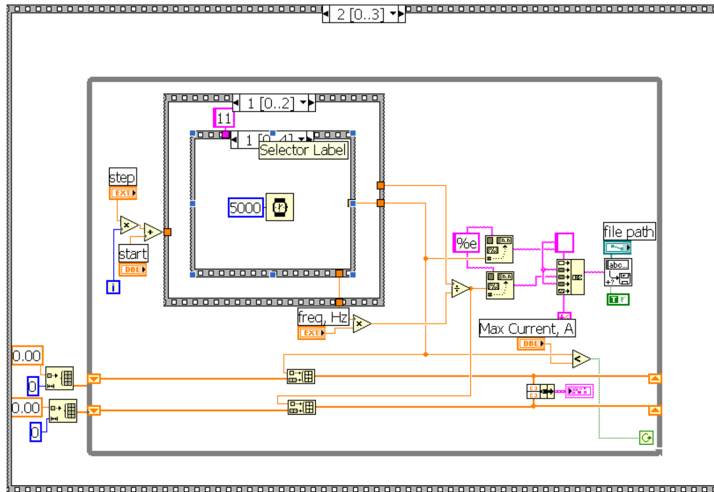
2 [0..3]
1 [0..2]
11
Selector Label
5000
step
start
freq, Hz
%e
Max Current, A
file path
0.00
0

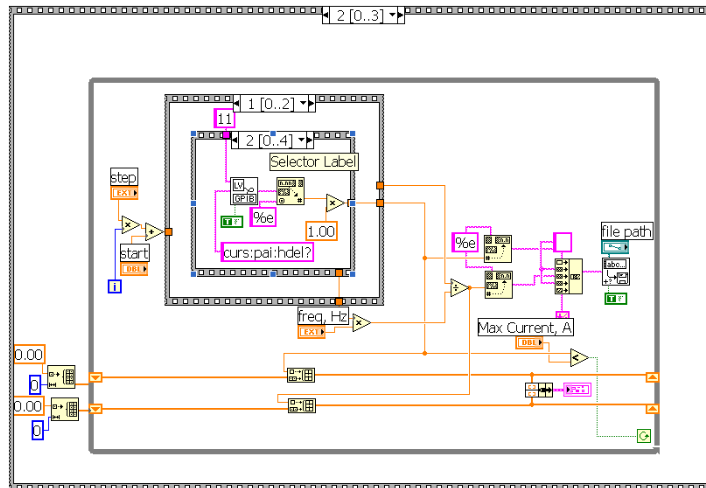
2 [0..3]
1 [0..2]
11
2 [0..4]
Selector Label
%e
1.00
curs:pai:hdel?
step
start
freq, Hz
Max Current, A
file path
0.00
0

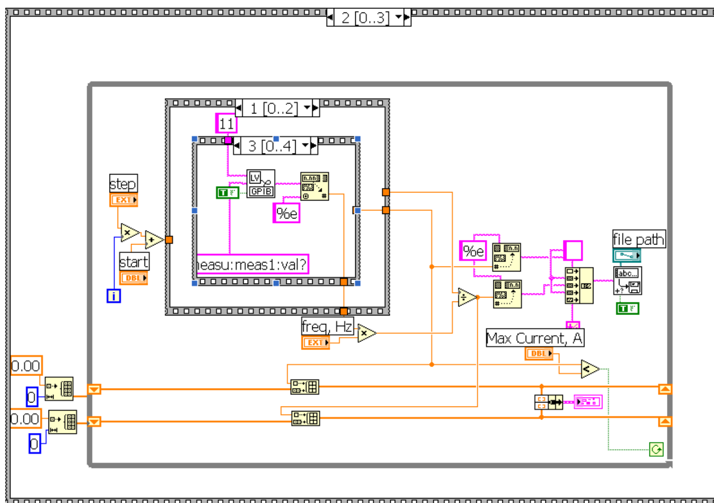
2 [0..3]
1 [0..2]
11
3 [0..4]
%e
easu:meas1:val?
step
start
freq, Hz
Max Current, A
file path
0.00
0

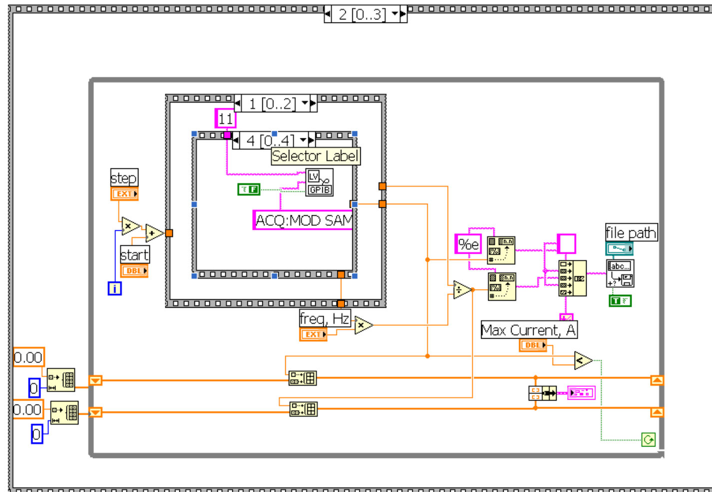
2 [0..3]
1 [0..2]
11
4 [0..4]
Selector Label
ACQ:MOD SAM
step
start
freq, Hz
%e
file path
Max Current, A
0.00
0
0.00
0

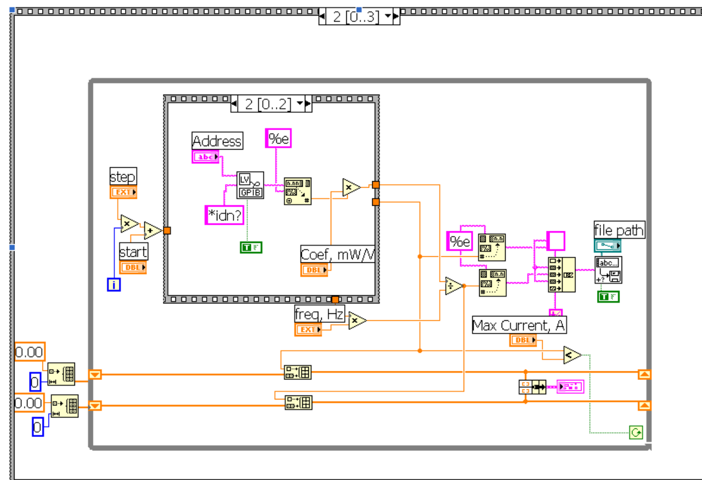
2 [0..3]
2 [0..2]
Address
%e
*idn?
step
start
Coef, mW/V
freq, Hz
%e
file path
Max Current, A
0.00
0
0.00
0

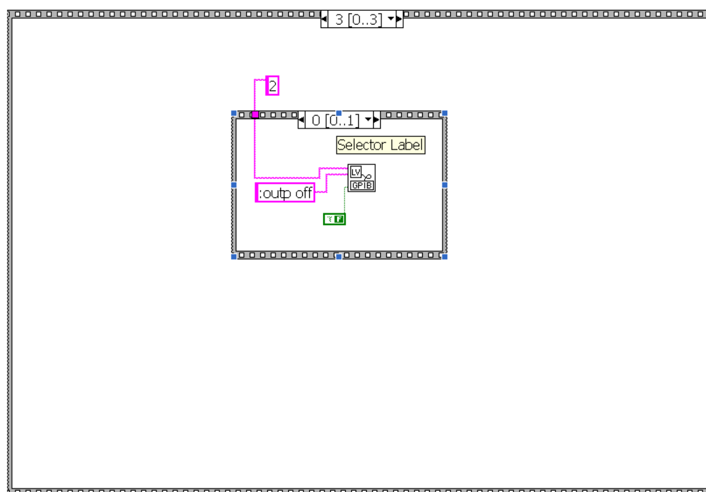
3 [0..3]
2
0 [0..1]
Selector Label
:outp off

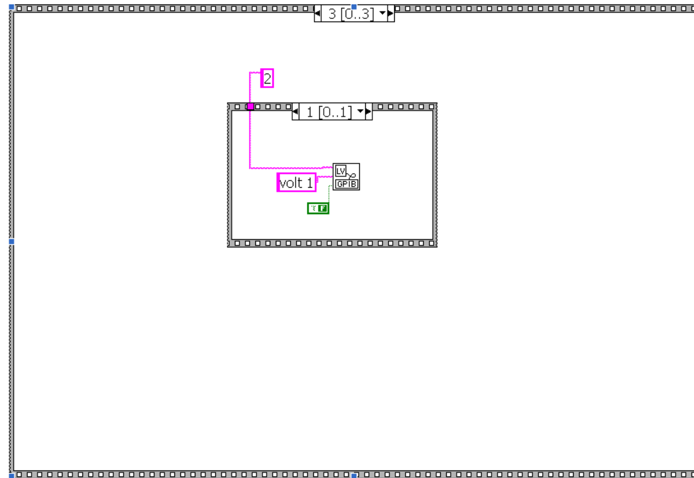
3 [0..3]
2
1 [0..1]
volt 1

III: Carrier Confinement in QWs with Quinary AlInGaAsSb as Waveguide Material

3.1 Introduction

Type-I quantum well (QW) diode lasers emitting around 2.7μm and operating at room temperature in continuous wave mode are in demand for laser spectroscopy, medical diagnostics and therapy, material processing, as well as infrared illumination and countermeasures. In most cases a broadened waveguide design approach was utilized for development of the type-I QW GaSb-based diode lasers [24]. The broadened waveguide approach was abandoned though for development of lasers with wavelength below 2.3 μm and reduced divergence in far field. In previously reported 2.7 μm emitting lasers the waveguide was broadened and made of quaternary AlGaAsSb alloy [25].

Here we present the results of fabrication and characterization of 2.7 μm GaSb based diode lasers with a new design. The total thickness of waveguide is reduced from 840 nm to 470nm and quinary AlInGaAsSb alloy is used as a waveguide/barrier material in place of quaternary AlGaAsSb. The waveguide thickness was optimized for maximum coupling between the optical field and the electrons in QWs. Increased overlap of the laser mode with p-cladding was balanced by reducing doping level in corresponding layer. New devices demonstrated threshold current densities as low as 200 A/cm^2 (for 2 mm long and 100 μm wide coated lasers) at room temperature in CW operation regime. CW

output power of 600 mW and peak power conversion efficiency of 10% were achieved at heatsink temperature of 16°C.

3.2 Heterostructure

The laser heterostructure was grown by solid-source molecular beam epitaxy at Stony Brook University using VEECO GEN-930 modular system equipped with valved cracker cells for both arsenic and antimony. The n-cladding layer was 2.0 μm wide $Al_{0.85}Ga_{0.15}As_{0.06}Sb_{0.94}$ doped with Te to nominal level of 10^{18} cm^{-3} (lower than nominal doping levels are expected in quaternary aluminum-containing alloys). The p-cladding $Al_{0.85}Ga_{0.15}As_{0.06}Sb_{0.94}$ layer was Be doped to $2\times10^{17}cm^{-3}$ over the first 0.5 μm, and to $8\times10^{17}cm^{-3}$ over the remaining 1 μm. Thus the doping level in the p-cladding was decreased compared to the level of $10^{18}cm^{-3}$ used in [25]. Graded bandgap heavily doped transition layers were introduced between the substrate and n-cladding and between the p-cladding and p-cap to assist carrier injection. Nominally undoped quinary $In_{0.2}Ga_{0.6}Al_{0.2}As_{0.2}Sb_{0.8}$ waveguide layer contained two 12 nm wide InGaAsSb QWs in the center. The QWs were separated by 50nm of waveguide material and contained about 47% of indium resulting into compressive strain of 1.7%. The wafer was processed into 100 μm wide gain-guided lasers. For measurement of the device modal gain spectra the 1-mm-long uncoated lasers were mounted epi-up onto Au-coated polished copper blocks. For CW characterization the facets were coated to reflect 3% (AR) and 95% (HR). The devices were In-soldered epi-

side down onto Au-coated polished copper blocks.

Figure 3.1 shows CW light-current and power efficiency characteristics of 2 mm long AR/HR coated devices measured at the coolant temperature of 16^0 C. The measured CW threshold current density was 200 A/cm^2, and near threshold external efficiency was 0.32 photons/electron. The maximum output power of 600 mW was achieved at 6.5 A of continuous wave current. The power conversion efficiency peaked at 10% at 1.5 A current. Improved (as compared to [24-25]) output power and power conversion efficiency correlate with nearly halved threshold current density (200 A/cm^2 versus 350 A/cm^2) and increased external efficiency (32% versus 26%).

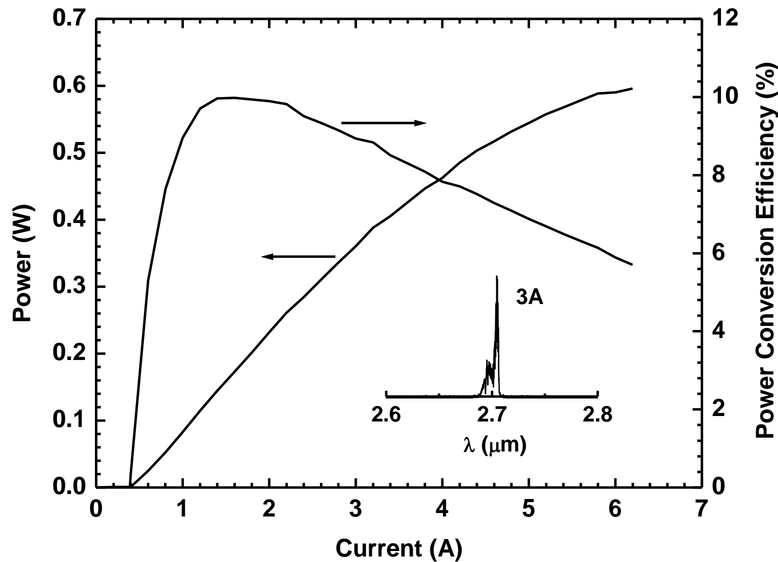

Figure 3.1 CW light-current and power-conversion characteristics of 2.7 μm emitting 2-mm-long AR/HR coated lasers; The inset shows the laser spectrum at 3A.

3.3 Experiment

The modal gain spectra (Figure 3.2) of 1 mm long uncoated device were measured for currents below thresholds using Hakki-Paoli method supplemented by the spatial filtering technique. The total optical loss of 17 cm^{-1} was determined from the long wavelength part of the gain spectra. Assuming the distributed mirror loss of 12 cm^{-1} for uncoated 1-mm-long devices, the internal optical loss can be estimated as 5 cm^{-1}. Calculated overlap of the modal field with p-cladding was about 15% in devices with 470nm waveguide width (8% for broadened waveguide devices from [25]). Relatively low value of the internal optical loss shows that the selected doping profile was effective in reducing free carrier absorption in the p-cladding layer. The voltage drop across laser heterostructure did not noticeably increase due to lower p-cladding doping and the devices demonstrated less than 1.7 V at 6.5 A of CW current.

The inset in Figure 3.2 shows the dependence of the peak modal gain on the under-threshold current. The rate of increase of peak modal gain with current is 110 cm^{-1}/A for 1-mm-long 100-μm-wide gain guided devices. The optical confinement factor for QWs is expected to improve by about 30% when the waveguide material is changed from $Al_{0.25}Ga_{0.75}As_{0.02}Sb_{0.98}$ to $Al_{0.2}In_{0.2}Ga_{0.6}As_{0.2}Sb_{0.8}$ and the total waveguide thickness is reduced from 840 nm to 470 nm. Increased optical confinement factor should enhance the device differential gain with respect to concentration. Additional improvement of the

device differential gain with respect to total device current stems from the fact that thermionic hole delocalization is expected to be mediated by the use of quinary barrier material [27-29]. Thus, improved hole localization and enhanced optical confinement factor lead to increased device differential gain. Improved differential gain and relatively low internal optical loss result in decreased threshold current density.

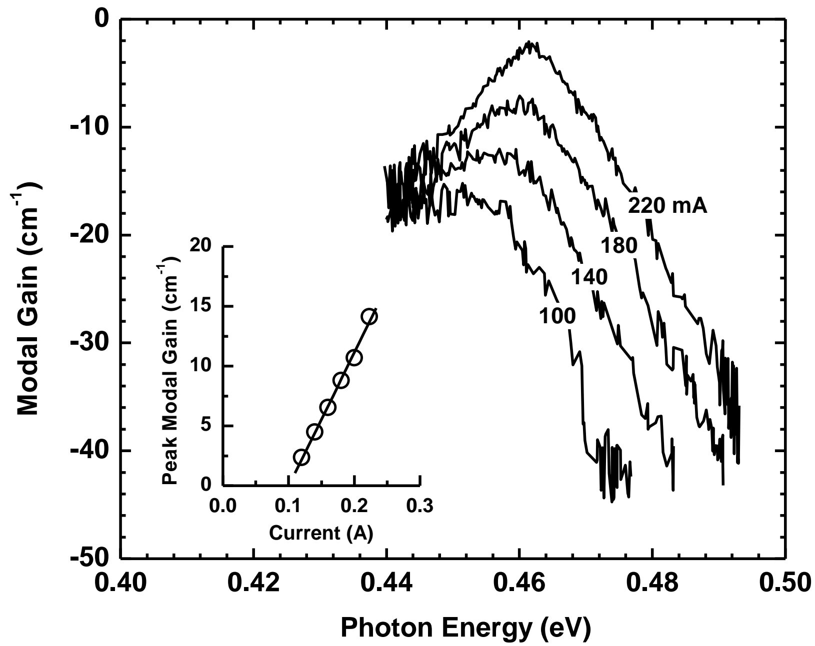

Figure 3.2 Current dependences of the modal gain spectra measured at 20°C for 1-mm-long uncoated devices. The inset shows the corresponding dependence of the peak modal gain on current.

Figure 3.3 shows the light-current characteristics measured in short pulse mode (200ns/10kHz) corresponding to negligible device heating (less than 0.5 W

of heat is dissipated on average at the maximum current). More than 3 W peak power was recorded at the current of 25 A. The measured fast axis beam profile in far field is shown in the inset of Figure 3.3. The devices show the fast axis divergence of 62^0 measured as full-width-at-half-maximum. Both parameters T_0 and T_1 characterizing thermal sensitivity of the device threshold current and slope efficiency were about 70K measured in temperature range from 20 to 50^0C.

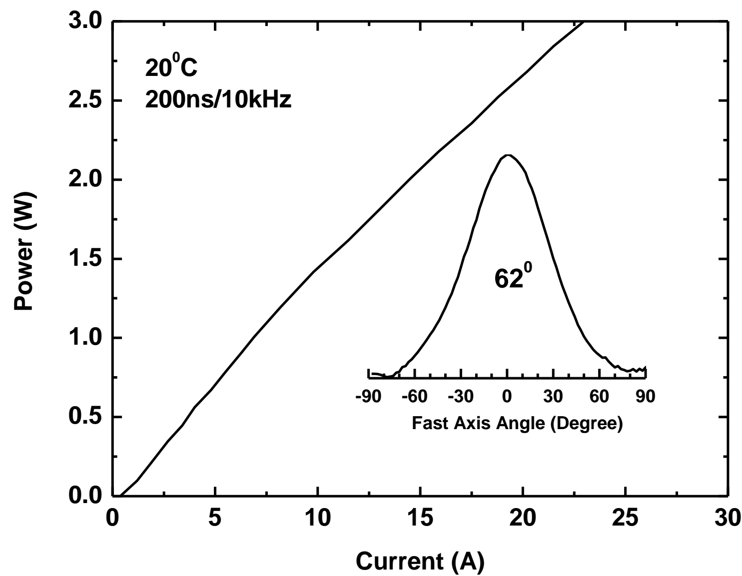

Figure 3.3 Pulsed light-current characteristics of 2.7 μm emitting 2-mm-long AR/HR coated lasers. The inset shows the fast axis far field divergence measured in CW regime.

3.4 Summary

2.7μm type-I GaSb-based laser diodes with quinary AlGaInAsSb waveguide/barrier material were developed and characterized. The devices were fabricated with waveguide width optimized for maximum QW optical

confinement. Threshold current density was 100 A/cm^2 per QW. Continuous wave output power of 600 mW was achieved at the heatsink temperature of 16^0 C and current of 6.5 A. Power conversion efficiency peaked at 10% at the current of 1.5 A. Devices demonstrate superior performance parameters as compared to previously reported 2.7 μm emitters having broadened waveguide made of the quaternary AlGaAsSb alloy.

3.5 Appendix

3.5.1 Fabrication steps:

1. SiN_x deposition (Trion PECVD)

   a. Sample preparation—HCl:H_2O=1:10 for 60 sec and dry with N_2 blast

   b. Ar Plasma (300mT/100 W/250 ℃/Ar 40 sccm/300 sec)

   c. NH_3 Plasma (300mT/100W/250 ℃/NH_3 40 sccm/600 sec)

   d. Deposition (600 mT/50 W/250 ℃/DES 16 sccm/NH_3 16 sccm/N_2 160 sccm)

2. Open window

   a. Lithography (Photoresist— NR1-3000PY, Developer—RD6)

      i. Spin— 4000 RPM for 40 sec

      ii. First bake—on hotplate at 130°C for 120 sec

      iii. Exposure—10 mW/cm^2 for 33 sec

      iv. Second bake—on hotplate at 110 ℃ for 80 sec

         -layer color eventually looks silver shiny after etching multiple layers of different colors (green, blue, etc.)

-remove photoresist completely (Aceton, Isopropanol, O_2 Plasma)

v. Develop—RD6 for 27 sec

b. Open Window with PECVD (300mT/100W/room temperature/CF_4 35sccm/O_2 5 sccm/until open~600 sec)

3. P-side metal deposition (Ti/Au)

a. Sample preparation—$NH_4OH:H_2O$=1:20 for 20 sec and dry with N_2 blast

b. E-beam metal deposition (Temescal BJD)

i. Wait till the pressure going down below 1.0×10^{-6} Torr

ii. Turn on heat, set the chamber temperature at 70 ℃, and wait again for an hour or two

iii. Ar plasma for 60 sec (1.0×10^{-4} Torr/Ar ~3 sccm/Beam Voltage 500 V/40 mA)

iv. Wait until the chamber temperature cool down to room temperature

v. Deposition

-Ti (200 Å)/ Au (1000 Å)

4. Lapping and polishing

a. Lap down substrate to 100-130 μm (use 3-5 μm aluminum oxide powder)

b. Polish the surface—use solution of 20 nm TiC (5 ml)/Water (50 ml)/Clorox (5-10 ml)

5. First n-side metal deposition (Ni/Au/Ge/Ni/Au)

a. Sample preparation—$NH_4OH:H_2O$=1:20 for 20 sec and dry with N_2 blast

b. E-beam metal deposition (Temescal BJD)

i. Wait till the pressure going down below 1.0×10^{-6} Torr

ii. Turn on heat, set the chamber temperature at 120 ℃, and wait again for an hour or two

iii. Ar plasma for 60 sec (1.0×10^{-4} Torr/Ar ~3 sccm/Beam Voltage 500 V/40 mA)

iv. Wait till the chamber temperature cool down to room temperature

v. Deposition

-Ni (50 Å)/Au (450 Å)/Ge (200 Å)/Ni (150 Å)/Au (2000 Å)

c. Rapid Thermal Processing (ramp 30 sec from room temperature to 250 ℃/stay at 250 ℃ for 120 sec)

-n-side metal layer diffuses in semiconductor and looks shiny white (becomes ohmic contact)

6. Second n-side metal deposition (Ti/Au)

a. Sample preparation—N_2 blast (dust off from surface)

b. E-beam metal deposition (Temescal BJD)

i. Wait till the pressure going down below 1.0×10^{-6} Torr

ii. Ar plasma for 60 sec (1.0×10^{-4} Torr/Ar ~3 sccm/Beam Voltage 500 V/40 mA)

iii. Wait till the chamber temperature cool down to room temperature

iv. Deposition

-Ti (200 Å)/Au (1000 Å)

3.5.2 Labview program for pulsed current-power characterization is the same as in chapter 2

3.5.3 Labview program for CW current-power-voltage characterization

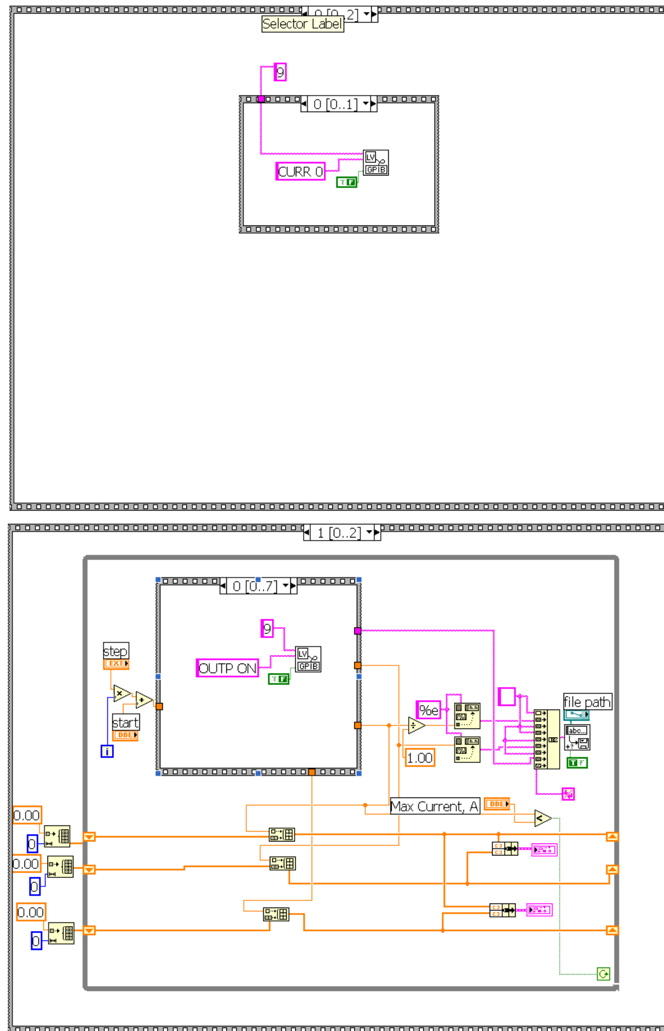

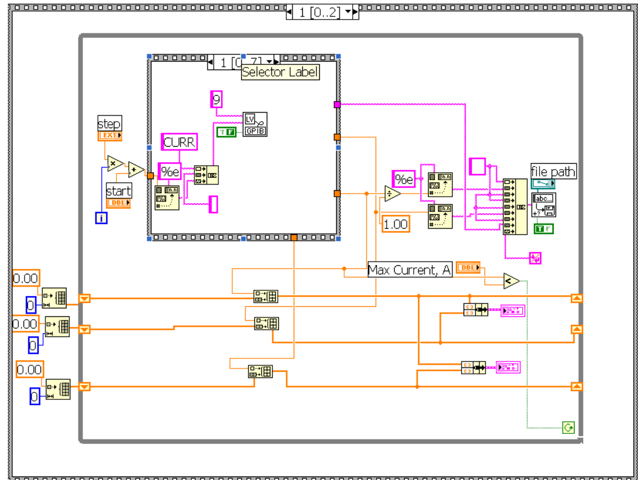
1 [0..2]
Selector Label
9
CURR
%e
step
start
%e
1.00
file path
Max Current, A
0.00
0
0.00
0
0.00
0

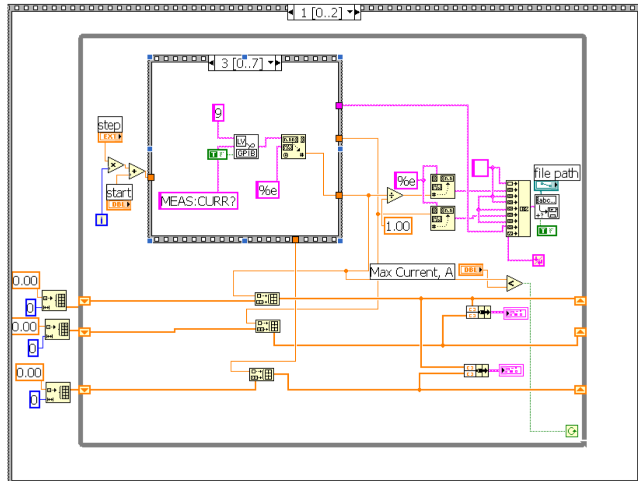
1 [0..2]
3 [0..7]
9
MEAS:CURR?
%e
step
start
%e
1.00
file path
Max Current, A
0.00
0
0.00
0
0.00
0

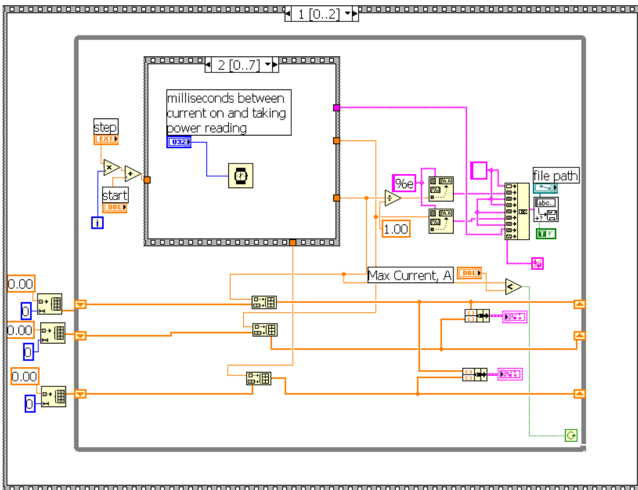
1 [0..2]
2 [0..7]
milliseconds between
current on and taking
power reading
step
start
%e
1.00
file path
Max Current, A
0.00
0
0.00
0
0.00
0

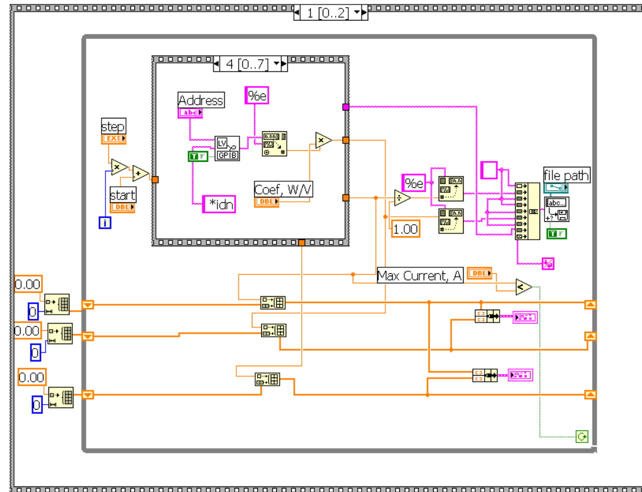
1 [0..2]
4 [0..7]
step
start
Address
%e
Coef, W/V
*idn
%e
1.00
file path
Max Current, A
0.00
0.00
0.00

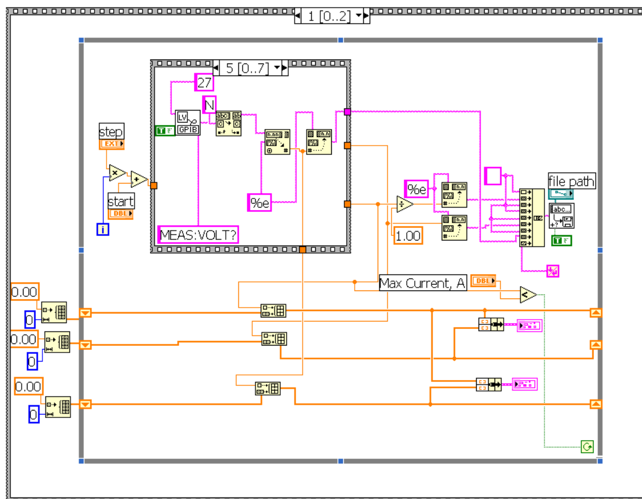
1 [0..2]
5 [0..7]
27
N
step
start
%e
MEAS:VOLT?
%e
1.00
file path
Max Current, A
0.00
0.00
0.00

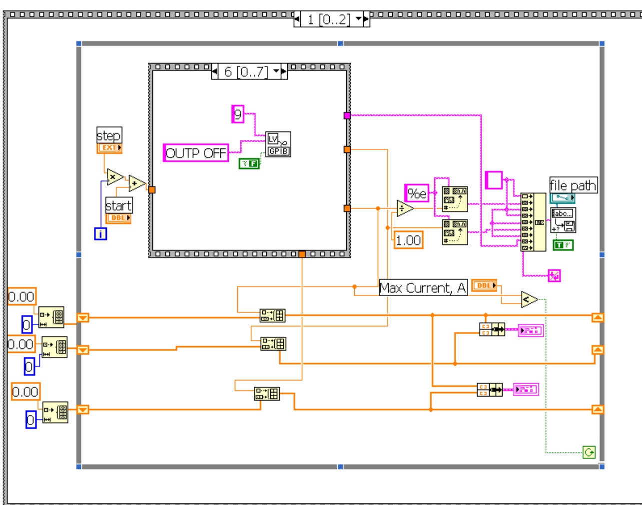
1 [0..2]
6 [0..7]
9
step
OUTP OFF
start
%e
1.00
file path
Max Current, A
0.00
0.00
0.00

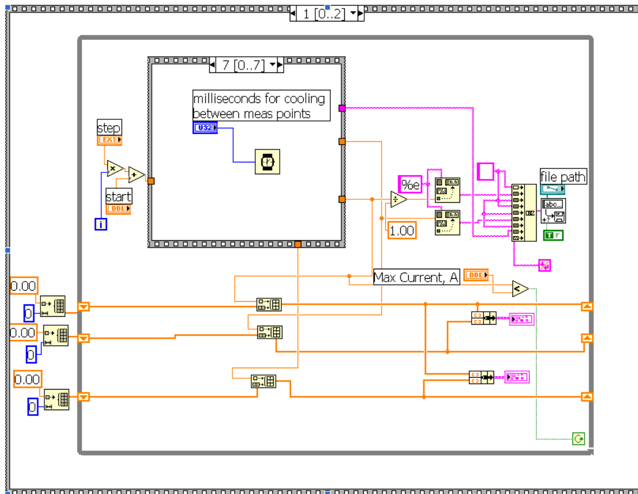
1 [0..2]
7 [0..7]
milliseconds for cooling
between meas points
step
start
%e
1.00
file path
Max Current, A
0.00
0.00
0.00
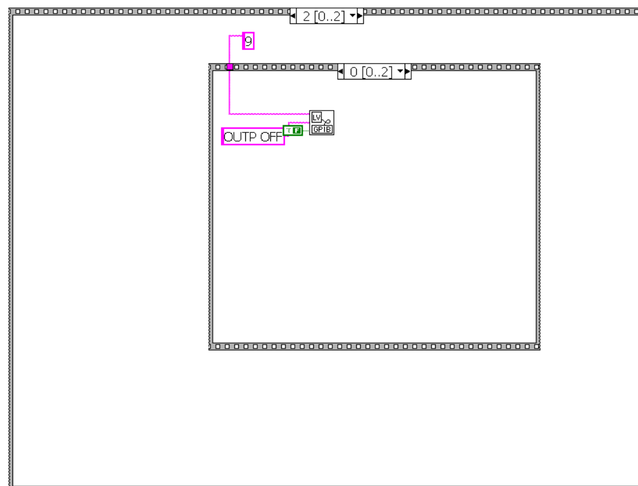
2 [0..2]
9
0 [0..2]
OUTP OFF
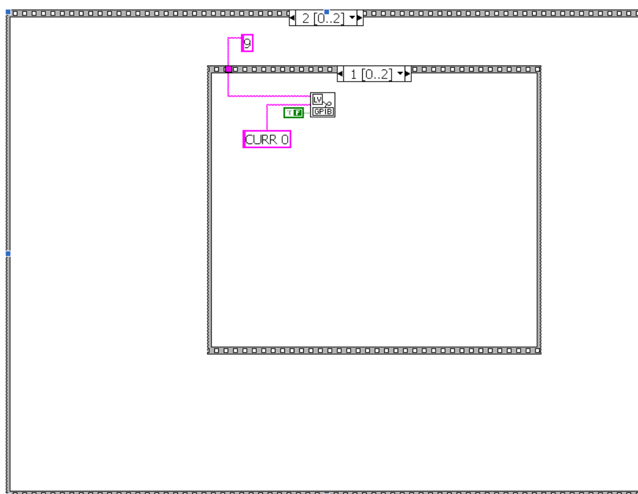
2 [0..2]
9
1 [0..2]
CURR 0

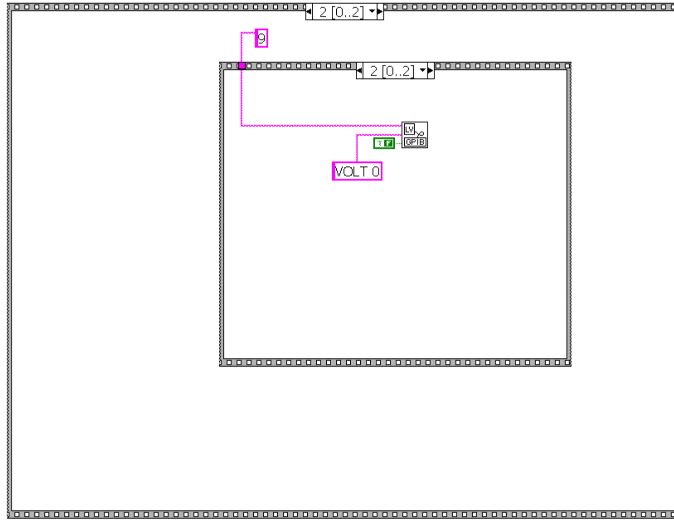
2 [0..2]
9
2 [0..2]
VOLT 0
GPIB

IV. Beam Properties

4.1High Power 2 μm Diode Lasers with Asymmetric Waveguide

4.1.1 Introduction

High-power diode lasers emitting near 2 μm are required for aesthetic surgery, infrared nerve stimulation, plastic welding as well as resonant pumping of the chromium doped II-VI semiconductors and holmium doped crystal/fiber lasers [30-33]. Broadened waveguide laser heterostructure design approach was successfully employed to improve efficiency of the 2 μm GaSb-based diode lasers [34]. Continuous wave (CW) output power of 1 W from 100-μm-wide aperture at 10^0 C was reported at 2.05 μm [35]. Power conversion efficiency reached about 23%. Broadened waveguide laser heterostructure design improves the device efficiency through reduction of the internal optical loss originating from overlap of the optical field with doped p-cladding. High power 2 μm diode lasers with broadened waveguide achieved threshold current densities of 100 A/cm^2 (50 A/cm^2 was reported for test device not showing the best output power) and initial

CW differential quantum efficiencies of 53% for 2-mm-long multimode devices [36].

Unless the waveguide core thickness is increased significantly the broadened waveguide lasers produce rather divergent beams in far field. GaSb-based 2 μm emitting diode lasers with about 1-μm-thick waveguide core demonstrated the fast axis far field distributions with full-width at half-maximum (FWHM) near 65 degrees. Reduction of the far field FWHM to below 50 degrees in broadened waveguide devices would call for waveguide core thickness in excess of 2 μm. Plausibly slow carrier transport in quaternary AlGaAsSb waveguide core material in combination with compromised optical coupling to active region can reduce laser efficiency and increase threshold current [37-38].

One of the alternative approaches would be to use narrow waveguides, i.e. spread optical wave into cladding regions expanding near field and narrowing the far field distribution. The effect of increased overlap of the optical field with p-cladding on internal losses can be mediated by reduction of the corresponding doping level. In order to prevent interaction of the laser field with heavily doped p-contact layers the p-cladding thickness should be increased as compared to broadened waveguide case. The likely penalty is increase in electrical and thermal resistance of the lasers. GaSb-based diode lasers emitting near 2 μm and utilizing narrow symmetric waveguide heterostructure designs demonstrated fast axis beam divergence of 44° FWHM. CW output power of 1.96 W from 150-μm-wide

aperture (corresponds to about 1.3 W from 100-μm-wide aperture) were reported at 17^0 C. Power conversion efficiency peaked at 26%. Initial CW differential quantum efficiency was about 50 % and threshold current density was about 200 A/cm^2 for 1-mm-long devices [39], i.e. these parameters were a bit compromised but still comparable to record 2 μm emitters with broadened waveguide.

In laser heterostructures with asymmetric waveguide the beam quality can be improved [40] by spreading optical mode selectively into n-cladding but not into p-cladding. Absorption cross section of free electrons is substantially lower than that of free holes [41], hence no substantial increase of the internal loss can be expected. Also, p-cladding thickness does not have to be increased to accommodate the mode interaction with heavily doped p-contact layers since penetration of the optical field into p-cladding is restricted. Asymmetric penetration of the modal field into p- and n-cladding can be achieved by using different compositions of the waveguide material on both sides of the active quantum wells. This approach was used and 2 μm emitting diode lasers with fast axis beam divergence of 30^0 FWHM were reported [42]. However, the maximum CW output power level was very low (below 50 mW) for unspecified reasons.

Here we improved the beam properties of the high power 2 μm emitting GaSb-based diode lasers by utilization of the waveguide structure with asymmetric claddings. The AlGaAsSb p-cladding contained about 90% of aluminum (similar to previously reported broadened waveguide 2 μm diode lasers

with record output power) while n-cladding aluminum content was reduced to 50%. Corresponding increase of n-cladding refractive index led to modal spreading into n-cladding layer resulting to reduced fast axis beam divergence. Devices with asymmetric claddings and variable waveguide core thicknesses ranging from above 800 down to below 300 nm were designed, fabricated and characterized. Reference structure with symmetric claddings and broadened waveguide was included into analysis as well. Fast axis beam divergence was successfully reduced from above 60 to below 40 degrees FWHM. High power 2 μm diode lasers with asymmetric claddings and fast axis beam divergence in the range 45-50 degrees demonstrated threshold current densities of 100 A/cm^2 and power conversion efficiency up to 28%. CW differential efficiencies of 55 and 45% were demonstrated for 1 and 2-mm-long high power 100-μm-wide coated emitters. Linear array and bundle of fiber coupled lasers were fabricated and characterized in CW under passive cooling to demonstrate the viability of the power scaling as required for applications.

Section 4.1.2 details the laser structure design, growth, fabrication and present initial characterization results. Section 4.1.3 describes the experimental studies of the trade-off between reduced far field divergence and laser threshold current and its temperature sensitivity. In Section 4.1.4, we present the results of CW characterization of the diode lasers and power scaled modules. Section 4.1.5 summarizes the results and observations.

4.1.2 Diode laser fabrication and preliminary characterization

Laser heterostructures were grown by solid-source molecular beam epitaxy on Tellurium doped GaSb substrates using Veeco GEN-930 modular system equipped with valved crackers for both As and Sb. Device active region contained two 12-nm-wide $In_{0.2}Ga_{0.8}Sb$ quantum wells (QW) spaced 20 nm apart by AlGaAsSb barrier. AlGaAsSb quaternary alloys lattice matched to GaSb were used as waveguide core and cladding materials. Graded band gap heavily doped transition layers were introduced between the substrate and n-cladding and between the p-cap and p-cladding to assist carrier injection. Tellurium and Beryllium were used as n and p dopants, respectively.

Wafers were processed into 100-μm-wide aperture multimode lasers. Uncoated 1-mm-long lasers were indium-soldered epi-side up onto gold coated copper blocks and characterized in pulsed (200ns/100kHz-1MHz) regime. For CW characterization the devices with 1- and 2-mm-long cavities and mirrors coated to reflect ~ 5 % (anti-reflection, AR) and 95 % (high-reflection, HR) were mounted epi-side down for more effective heat removal.

Laser heterostructures with different width and composition of the core and claddings materials were designed, fabricated and characterized. Table 4.1 lists the parameters of the six laser heterostructures studied.

Refractive index step between $Al_{0.9}Ga_{0.1}As_{0.07}Sb_{0.93}$ claddings and $Al_{0.25}Ga_{0.75}As_{0.02}Sb_{0.98}$ core in symmetric broadened waveguide laser structure 1

can be estimated as 0.45 for 2 μm light [43]. Figure 4.1.1a plots schematically the calculated band alignment [44] and near field distribution.

	p-clad		core		n-clad	
	% Al	nm	% Al	nm	% Al	nm
1	90	1500	25	850	90	1500
2	90	1500	25	850	50	2000
3	90	1500	25	550	50	2000
4	90	1500	25	350	50	2000
5	90	1500	25	250	50	2500
6	90	1000	30	450	50	2500

Table 4.1 Composition and width of the claddings and core layers of the 2 μm emitting laser heterostructures studied.

Broad 850 nm waveguide core and large refractive index step between core and claddings effectively confine optical mode leading to small (about 4 %) overlap with p-cladding. Laser diodes of that design demonstrate threshold current density of about 150 mA for 1-mm-long, 100-μm-wide cavity with uncoated mirrors (Figure 4.1.2). Parameter T_0 characterizing exponential dependence of the laser threshold on temperature exceeds 100 K. Differential quantum efficiency estimated from light-current characteristics is above 50 %. Fast axis beam divergence of this otherwise decent 2 μm emitting laser is above

60 degrees FWHM (Figure 4.1.3, structure 1). The divergence above 60 degrees implies that the collecting optics with numerical aperture 0.5 or bigger is required to utilize the power produced by diode laser.

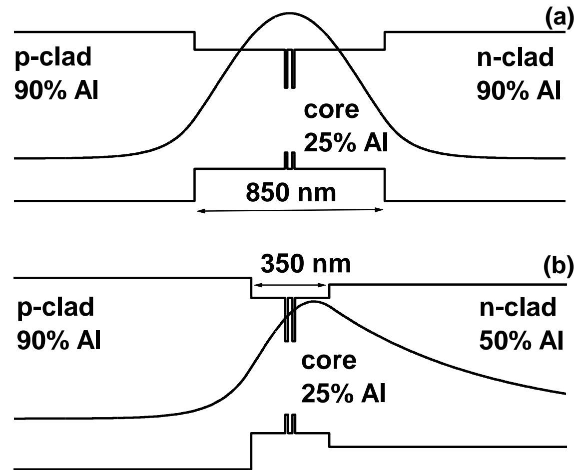

Figure 4.1.1 Calculated band alignment diagram and transverse near field distribution of (a) symmetric broadened waveguide laser structure 1 and (b) asymmetric narrow waveguide laser structure.

Change of the composition of the n-cladding from $Al_{0.9}Ga_{0.1}As_{0.07}Sb_{0.93}$ to $Al_{0.5}Ga_{0.5}As_{0.03}Sb_{0.97}$, reduces the refractive index step between n-cladding and waveguide core down to about 0.2. The resulting waveguide asymmetry leads to spreading of the laser mode into n-cladding but keeps overlap with p-cladding below 8 % even for narrow 350-nm wide core (Figure 4.1.1b). The far field distributing narrows down by about 5 degrees for broadened waveguide laser structure 2 with asymmetric waveguide. No penalty in laser operating parameters can be observed in structure 2 as compared to structure 1, i.e. one can assume that

conduction and valence band offsets between waveguide core and 50% aluminum cladding materials are still adequate.

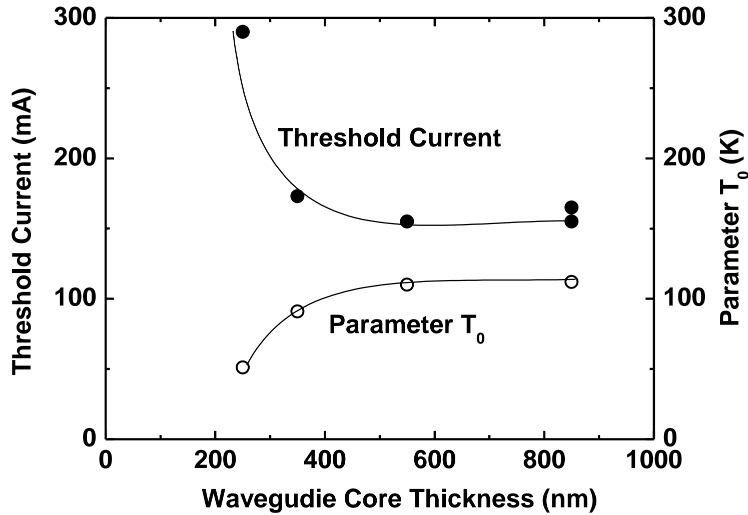

Figure 4.1.2 Dependences of the threshold current at 20 ^{0}C (solid circles) and parameter T_0 (open circles) on waveguide core thickness (lines are guide for eye only). Measurements were performed under pulsed excitation (200ns/100kHz) for 1-mm-long, 100-μm-wide uncoated lasers mounted epi-side up onto gold coated copper blocks.

Reduction of the waveguide core width in laser structure with asymmetric claddings from 850 nm to 550 (structure 3), then to 350 (structure 4) and finally down to 250 nm (structure 5) is accompanied by gradual improvement of the beam quality. Figure 4.3 shows that the FWHM maximum of the far field reduces to below 40 degrees thanks to progressing expansion of the modal field into n-cladding direction. Favorable reduction of the beam divergence eventually brings unfavorable degradation of the laser parameters (Figure 4.1.2). Threshold current increases up to 300 mA and parameter T_0 decreases down to 50 K for structure 5

with the narrowest waveguide core. Lasers with structures 3 and 4 demonstrate fast axis beam divergences below 50 and 45 degrees, respectively, and do not experience dramatic degradation of these important parameters (Figure 4.1.2).

4.1.3 Experimental studies of the laser gain and loss

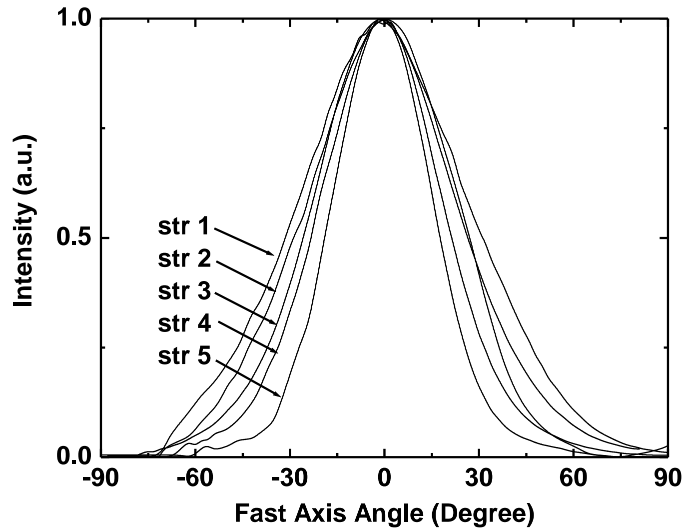

Figure 4.1.3 Measured fast axis far field distributions of 2 μm emitting laser diodes with 1-mm-long, 100-μm-wide uncoated cavities. Structure numbers correspond to table 4.1.

Figure 4.1.3 demonstrates that the reduction of the waveguide core width in diode lasers with asymmetric claddings improves the beam quality. Twofold increase of the threshold current density in lasers with waveguide core width of 250 nm can be explained by: (a) reduction of the coupling between double-QW active region and laser mode; (b) modal leakage into high-index GaSb substrate [45]. Both (a) and (b) are caused by spreading of the optical field into direction of n-cladding. Double-QW optical confinement factor gets decreased gradually with

narrowing waveguide core since modal volume grows and mode maximum shifts from waveguide core center. Eventually, waveguide core width can be reduced below cut-off value (estimated to be about 200 nm) and no mode could be supported. Progressing increase of the field amplitude in the n-cladding would necessitate increase of the n-cladding thickness when decreasing core width to prevent modal leakage into the substrate. Reduction of the optical confinement, increase of the internal optical loss as well as modal leakage into the substrate can be identified from modal gain spectral measurements.

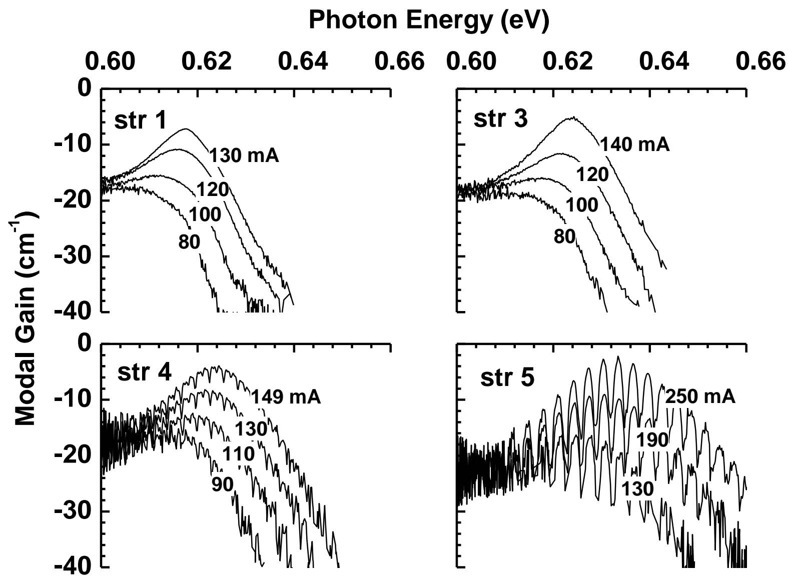

Figure 4.1.4 Modal gain spectra measured at several under threshold currents for 1-mm-long, 100-μm-wide uncoated lasers. Structure numbers correspond to table 4.1.

Modal gain spectra were measured for multimode diode lasers using Hakki-Paoli method supplemented by the spatial filtering optics. Figure 4.1.4 plots

selected spectra obtained at several under threshold currents for diode lasers with structures 1, 3, 4 and 5.

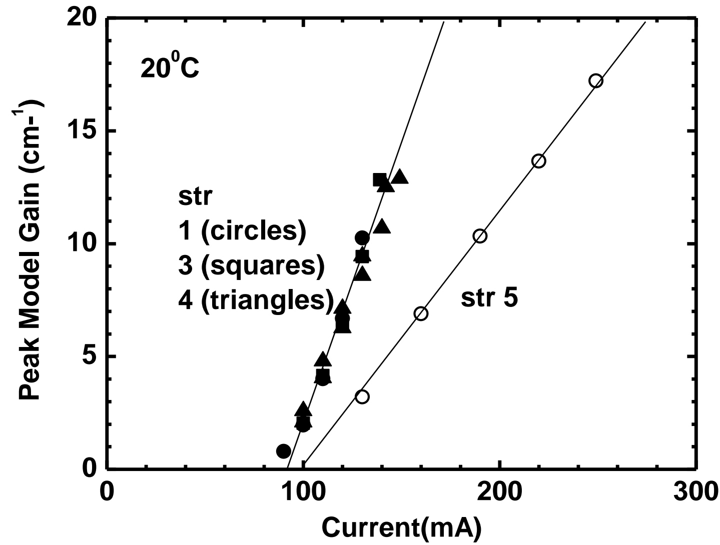

Figure 4.1.5 Current dependences of the peak modal gain measured for lasers with structures 1, 3, 4 and 5 (Table 4.1).

In the long-wavelength part of the spectra, where the material gain is zero, the modal gain is nearly equal to total loss [46]. Mirror loss of 1-mm-long uncoated lasers is about 12 cm^{-1}. Values of the internal optical losses can be estimated to be 5 - 7 cm^{-1} for structures with 850, 550 and 350 nm wide waveguide cores. Indeed, no significant increase of the internal optical loss is expected since the overlap of the optical field with p-cladding remains restricted in asymmetric narrow waveguide laser heterostructures (compare Figures 4.1.1a and 4.1.1b). However, the internal optical loss in structure 5 does increase up to 8

- 10 cm^{-1}. The loss increase is also accompanied by pronounced periodic modulation of the modal gain spectra (Figure 4.1.4). The modulation is indication of the strong modal leakage into the substrate despite increased n-cladding thickness up to 2500 nm (Table 4.1). The slight hint of the modulation can be seen in gain spectra for structure 4 implying that the n-cladding thickness should already have been increased above 2000 nm in lasers with 350 nm core.

Figure 4.1.5 plots current dependencies of the peak modal gain for structures 1, 3, 4 and 5. Transparency current is 90 - 100 mA regardless of laser waveguide heterostructure geometry. Indeed, the devices with identical double-QW active regions are expected to have very similar transparency currents unless injection efficiency changes with waveguide geometry. Differential gain with respect to current is directly proportional to optical confinement factor and thus is expected to be decreasing together with waveguide core width. Marginal decrease of the differential gain is observed with reduction of the waveguide width from 850nm down to 350 nm. Twofold reduction of the differential gain is observed in structure 5 with core width of 250 nm. Sharp drop of the optical confinement factor with reduction of the waveguide width in the range of narrow waveguides can account for this observation. Estimated ratio of the confinement factors of structures 1 and 5 is about 2 indeed.

Reduced differential gain can explain the degradation of the parameter T_0 is devices with the narrowest waveguides (Figure 4.1.2). Increased threshold carrier

concentrations are expected in devices with reduced optical confinement and thus lowered differential gain. The indication of the increased threshold carrier concentration can be recognized in increased width of the gain spectra near threshold of structure 4 and especially structure 5 (Figure 4.1.4). Carrier delocalization and nonradiative Auger recombination are expected to enhance their effect on laser threshold current with increase of threshold carrier concentration. Both of these adverse phenomena boost the thermal sensitivity of the laser threshold and hence degrade parameter T_0.

Unless thick n-cladding can be afforded and optical confinement is somehow improved the use of the waveguide width below 350 nm is clearly undesirable. Already for lasers with 350 nm wide waveguide core the indications of the modal leakage and reduction of the optical confinement factor start to appear in Figures 4.1.4 – 4.1.5. To accommodate for the possible associated penalties in structure 4 the structure 6 was designed, fabricated and characterized. In this structure the n-cladding thickness was increased up to 2500 nm, core thickness was 450nm, QWs were shifted to n-cladding side to coincide with calculated modal maximum (Figure 4.1.1b) and 30 % aluminum in waveguide was used to facilitate carrier confinement in active QWs of 2 μm lasers [47]. The wafer was processed and characterized in a manner similar to structures from Figure 4.1.2 except the top cladding material was wet etched outside 100-μm-wide stripes. This was done to eliminate any lateral current spreading and achieve

sharp lasing transition near threshold. For 1-mm-long uncoated devices operated in pulsed regime at the heatsink temperature of 20^0C, the threshold current density was 100 mA/cm^2. Differential quantum efficiency was 60%. The gain spectra (not shown) of devices with structure 6 did not show any modulation, i.e. there were no modal leakage into substrate. Internal optical losses of about 5 cm^{-1} were estimated from Hakki-Paoli measurements.

4.1.4 Room temperature CW operation

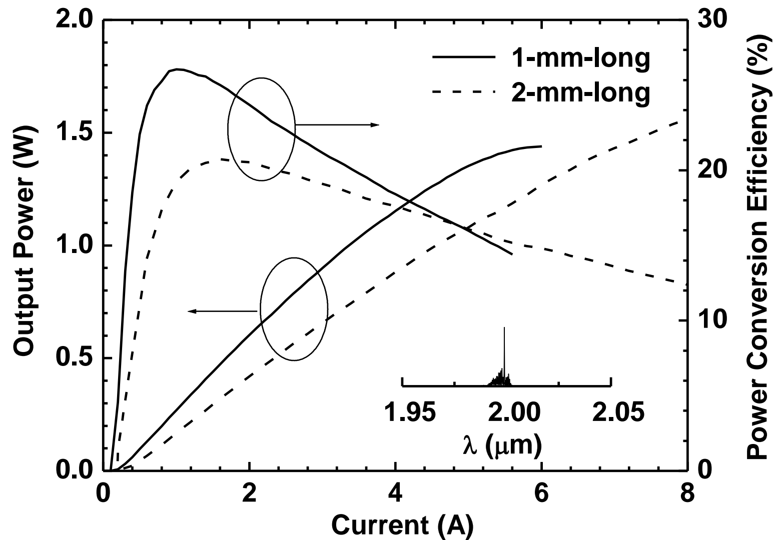

Figure 4.1.6 CW power and power conversion characteristics measured at 20°C for 1- and 2-mm-long, AR/HR coated lasers with structure 3. Inset shows laser spectrum.

Measurement of CW output power was performed for diode lasers and their arrays indium-soldered epi-side down onto gold-coated copper blocks that were bolted to thermoelectrically cooled (TEC) copper surface. The heat from the other

side of the TEC was removed by flowing water. The stage was able to drive up to 100 W of heat that was ample for individual lasers but insufficient to drive currents in excess of 60A through linear arrays.

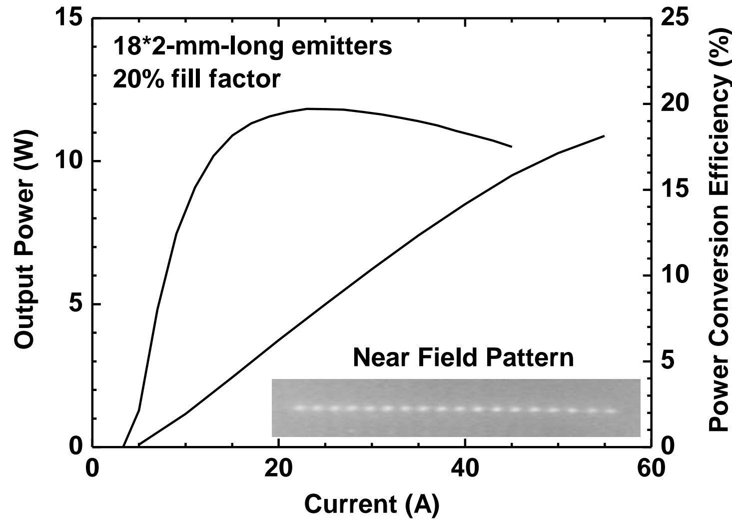

Figure 4.1.7 CW power and power conversion characteristics measured at 20^0C for 2-mm-long, AR/HR coated 18-element linear laser array with structure 3. The array fill-factor was 20%, i.e. 100-μm-wide emitters with 500-μm pitch. The inset shows the corresponding near field.

Diode lasers with structure 3 (far field divergence with FWHM of 50 degrees) generate above 1.5 W of CW power and demonstrate peak power conversion efficiency in excess of 28% (Figure 4.1.6). Linear laser array with fill factor of 20% composed of eighteen 2-mm-long emitters with structure generated above 11 W at 20^0C at current of 55 A (Figure 4.1.7). Power conversion efficiency was above 20% in peak and above 15% at maximum power level. Driving current and output power were limited by TEC stage heat removal capabilities.

Diode lasers with structure 4 (far field divergence with FWHM of 44 degrees) generate 1.4 W of CW power but peak power conversion efficiency was below 20% (Figure 4.1.8). Smaller value of the output power and efficiency is associated with higher optical loss and stronger temperature sensitivity of the threshold (Figure 4.1.4 and 4.1.2). Still the devices were producing more than watt of 2 μm power at power conversion efficiency better than 10%.

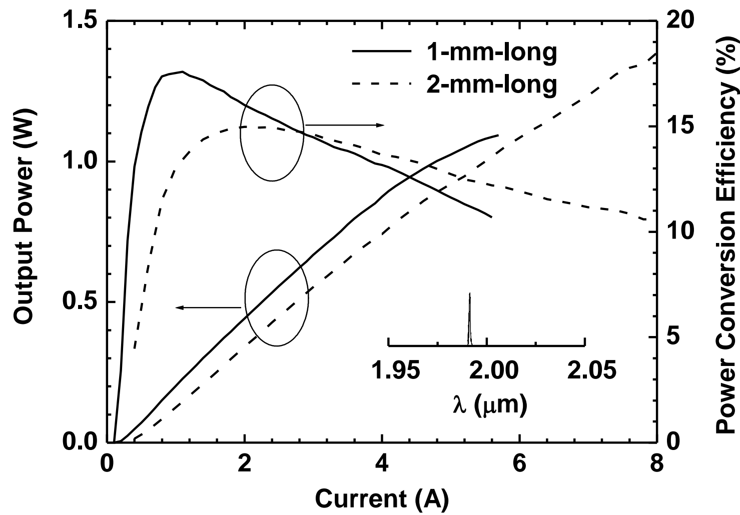

Figure 4.1.8 CW power and power conversion characteristics measured at 20^0C for 1- and 2-mm-long, AR/HR coated lasers with structure 4. Inset shows laser spectrum.

Seven 2-mm-long AR/HR coated single emitters of structure 4 were epi-down mounted onto Au-coated BeO blocks and connected in series. Output light was collected by a cylindrical micro-lens in front of each emitter into seven multimode silica fibers with the core diameter of 100 μm. No optimization of the collecting optics was done for the particular 2 μm laser technology. More than 3

W of CW power was collected from the other end of the fiber bundle (Figure 4.1.9).

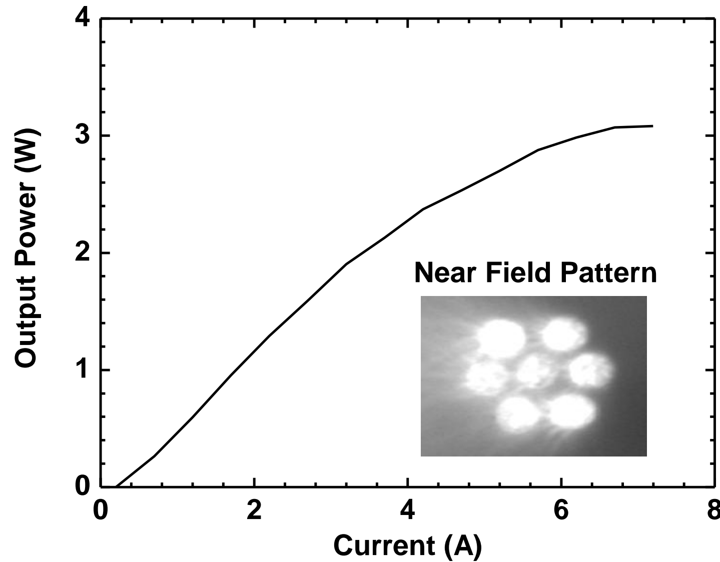

Figure 4.1.9 Fiber coupled CW power generated by seven 2-mm-long AR/HR coated devices with structure 4. The inset shows the near field image of the fiber bundle output.

For structure 6 with QWs shifted closer to the n-cladding layer, as low as 100 A/cm^2 and 85 A/cm^2 of CW threshold current density, at 20^{0}C, were achieved for 1- and 2-mm-long AR/HR coated lasers, respectively. Output power above 1.3 W was generated at 8 A. Power conversion efficiency peaked above 25% but rapidly decreased with current due to voltage drop across series resistance. Increase of the series resistance in structure 6 as compared to structure 3, for instance, is not fully understood. The excessive voltage drop across laser heterostructure can be ascribed to reduced doping in p-cladding layer (10^{17} cm^{-3}

of Be was used in p-clad of structure 6 as compared to 2×10^{17} cm^{-3} in structures 1 - 4). This model would have to assume rather low hole mobility though. Another possible explanation is adverse variation of the substrate doping level and associated increase of the n-contact resistance.

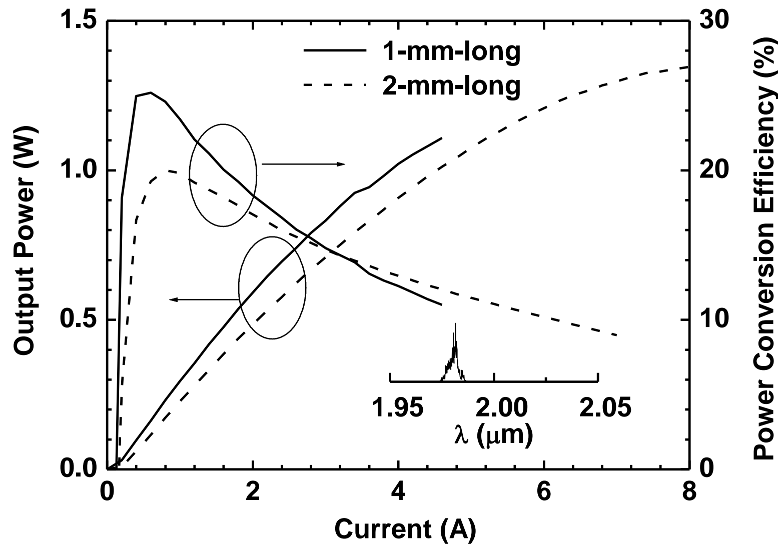

Figure 4.1.10 CW power and power conversion characteristics measured at 20^{0}C for 1- and 2-mm-long, AR/HR coated lasers with structure 6. Inset shows laser spectrum.

4.1.5 Summary

Asymmetric narrow waveguide approach to design of 2 μm high power laser emitters was utilized. Fast axis far field beam divergence was reduced from above 60 degrees to below 40 degrees when the symmetric broadened waveguide laser heterostructure was changed to asymmetric narrowed waveguide one. Experiment showed that the waveguide asymmetry restricted modal penetration

into p-cladding maintaining the internal optical loss at level achieved in broadened waveguide laser heterostructures.

The penalty associated with reduced optical confinement and modal leakage into high index GaSb substrate becomes apparent when waveguide core reduced below 350 nm to obtain beam divergence below 40 degrees. Devices with 45-50 degree fast axis beam divergence do not suffer from significant performance degradation. Corresponding single emitters with 100-μm-wide output aperture generate above 1 W at 20 ^{0}C of 2 μm optical power with power conversion efficiency exceeding 15 % at maximum power level and peaking at 28%. Linear laser arrays generate above 10 W of CW power. More than 3 W of CW power was demonstrated from fiber bundle containing seven 100-μm diameter silica fibers.

Achievement of the similar high power CW with beam divergence below 40 degrees is possible provided the n-cladding layer thickness is increased sufficiently to eliminate modal leakage into the substrate and QW active region is adjusted (shifted to n-cladding and number of QWs is increased) to accommodate for reduced optical confinement. By shifting QWs closer toward the n-cladding layer and utilizing wet etching to confine the current laterally the threshold current density as low as 85 mA/cm^2 was achieved for 2-mm-long AR/HR coated high power lasers generating above 1 W of CW power.

4.2 1.95 µm Diode Lasers with Asymmetric Waveguide and Improved Properties

4.2.1 Introduction

Power produced by diode lasers emitting around 1.95 µm can be used either directly or to achieve resonant pumping of 2 µm emitting solid state or fiber laser hosts. Holmium ions in silica or fluoride glass fibers have wide (well above 10 nm) $^5I_8 \rightarrow {}^5I_7$ absorption band centered near 1.95 µm, see, for instance [48]. This band has nearly twofold higher absorption cross section than that of traditionally used $^5I_8 \rightarrow {}^5I_6$ band near 1.15 µm. Pumping of the corresponding 2.1 µm fiber lasers near 1.95 µm will lead to Stokes defect below 50 meV — clearly an advantage for high energy laser systems. Continuous wave (cw) operation of the diode lasers with Watt level output power is required for pumping of this quasi three level fiber laser. The brightness of the pumping diodes should be maximized to reduce overall system complexity and cost.

4.2.2 Laser heterostructures

The laser heterostructure was grown by solid-source molecular beam epitaxy. Figure 4.2.1(a) shows calculated band alignment and near field distribution. The active region contained three 7 nm wide compressively strained

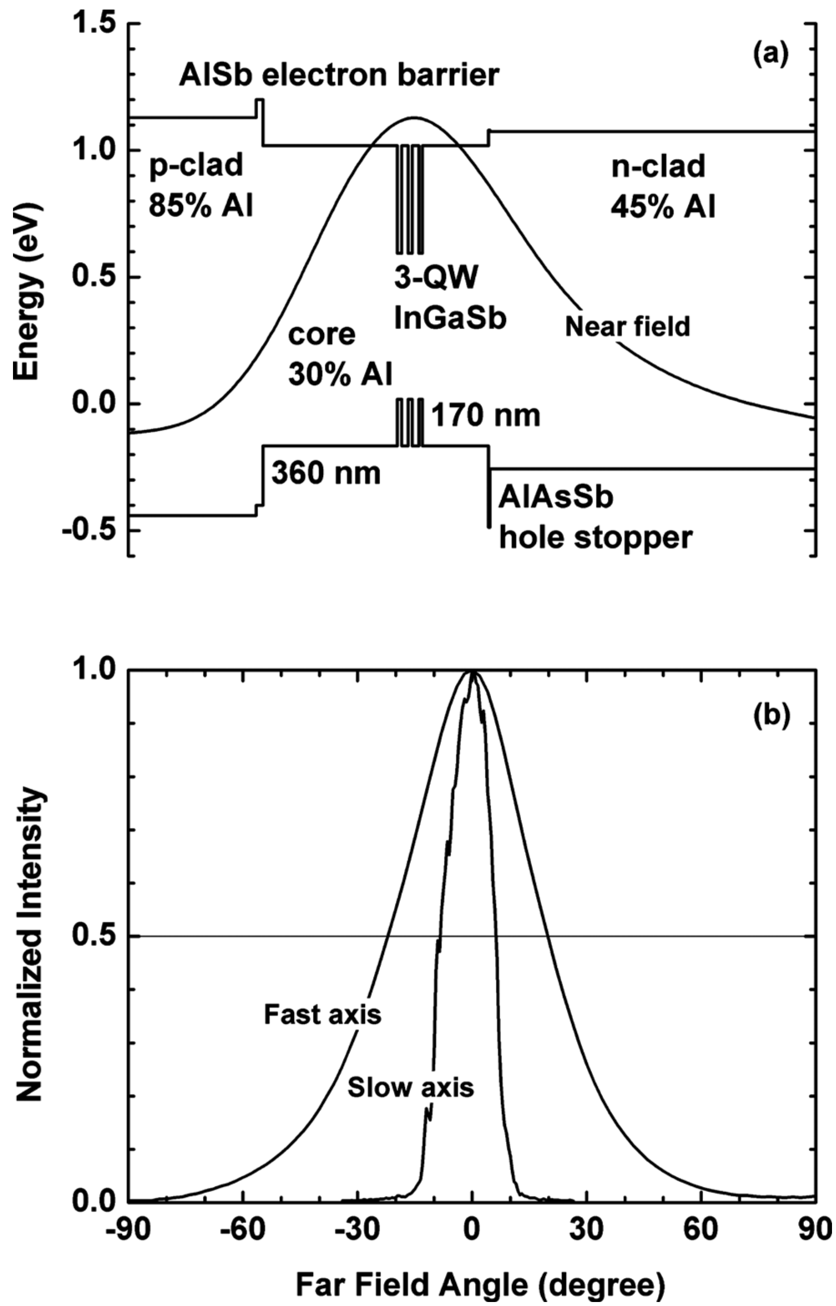

Figure. 4.2.1 (a) Calculated band diagram of the laser heterostructure overlapped with near field distribution; (b) corresponding far field patterns measured in slow and fast axis directions.

$In_{0.25}Ga_{0.75}Sb$ QWs separated by 20 nm thick $Al_{0.3}Ga_{0.7}As_{0.03}Sb_{0.97}$ barriers. The

active region was placed into the maximum of the near field distribution. The 360 and 170 nm thick $Al_{0.3}Ga_{0.7}As_{0.03}Sb_{0.97}$ layers separated active region from p- and n-claddings. 1 μm thick $Al_{0.85}Ga_{0.15}As_{0.06}Sb_{0.94}$ p-cladding layer was Be doped to 10^{17} cm^{-3} over the 400 nm adjacent to waveguide core and to 10^{18} cm^{-3} over the remaining 600 nm. 2500 nm thick $Al_{0.45}Ga_{0.55}As_{0.04}Sb_{0.96}$ n-cladding layer was Te doped to nominal 10^{18} cm^{-3}. 20 nm thick AlSb and 5 nm thick $AlAs_{0.1}Sb_{0.9}$ layers were inserted between waveguide core and n- and p-cladding layers, respectively.

4.2.3 Experiment

The wafer was processed into 100 μm wide isolator confined ridge waveguide lasers. Ridges waveguides were fabricated by wet-etching of the cap and p-cladding layers outside of the current stripe. For optical gain measurements and initial pulsed characterization the 1 mm long uncoated lasers were mounted episide up. For cw characterization, 3 mm long devices were coated to reflect below 5% [antireflection (AR)] and 95% [high-reflection (HR)] and were indium-soldered epi-side down onto gold plated polished copper blocks.

Current independent far field patterns with beam divergences of 42 ° and 15 ° FWHM were measured in fast and slow axes, respectively [Figure 4.2.1(b)]. Stable multimode slow axis far field pattern is ascribed to strong index guiding achieved in lateral deeply etched ridge waveguide. We explain the low divergence of only 42 ° observed in diffraction limited fast axis direction by enhanced spot size in the corresponding near field. Transverse spot size enhancement was

achieved by expanding the modal field into n-cladding. Utilization of the cladding materials with reduced aluminum contents (45% in n-cladding versus 85% in p-cladding) formed the asymmetric waveguide structure. The estimated refractive index step between waveguide core and p-cladding is about 0.4 while that between core and n-cladding is only 0.1 [49]. Reduction in the aluminum content in n-cladding from 85% to 45% was accompanied by undesired reduction in the corresponding valence band offset with core alloy by about 200 meV [50]. To balance the reduced valence band offset the hole stopper layer was introduced. Electron stopper layer was added on p-side to further reinforce carrier confinement in the waveguide core [51].

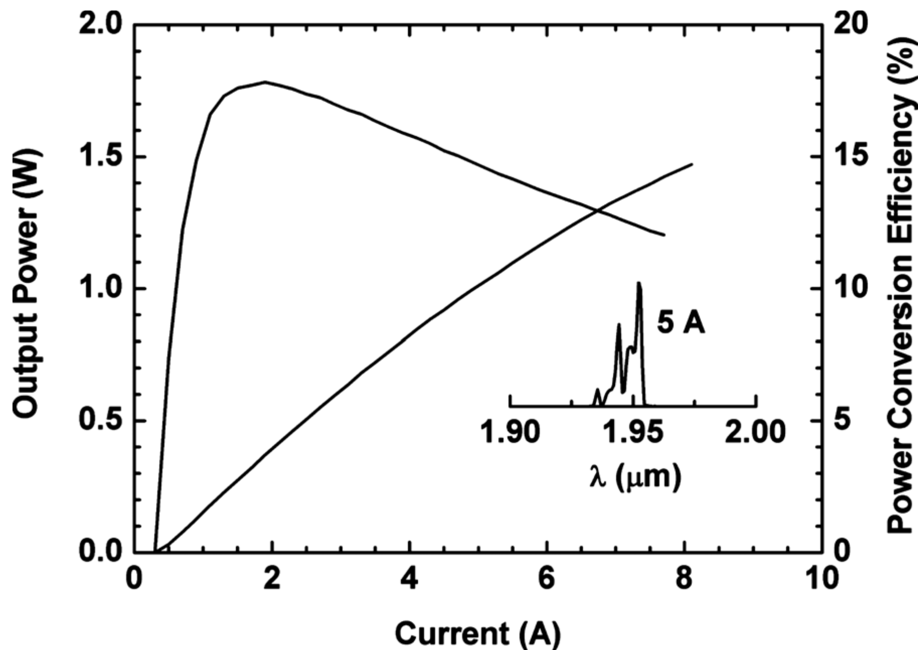

Figure 4.2.2 cw power and power conversion characteristics of 100 μm wide 3 mm long AR/HR coated devices measured at 20 ℃. Inset shows laser spectrum at 5 A.

Figure 4.2.2 plots device power and power conversion characteristics. Maximum cw output power of about 1.5 W were measured for 100 μm wide 3 mm long coated lasers at 20 ℃. Power conversion efficiency remained above 11% at maximum output power level. The differential quantum efficiency was estimated to be around 40%. Package thermal resistance of about 4 K/W was determined from comparison of laser spectra measured in cw at fixed temperature and in short pulse mode at different temperatures. This value suggests that the laser active region overheats only by 50 K up to the maximum output power level.

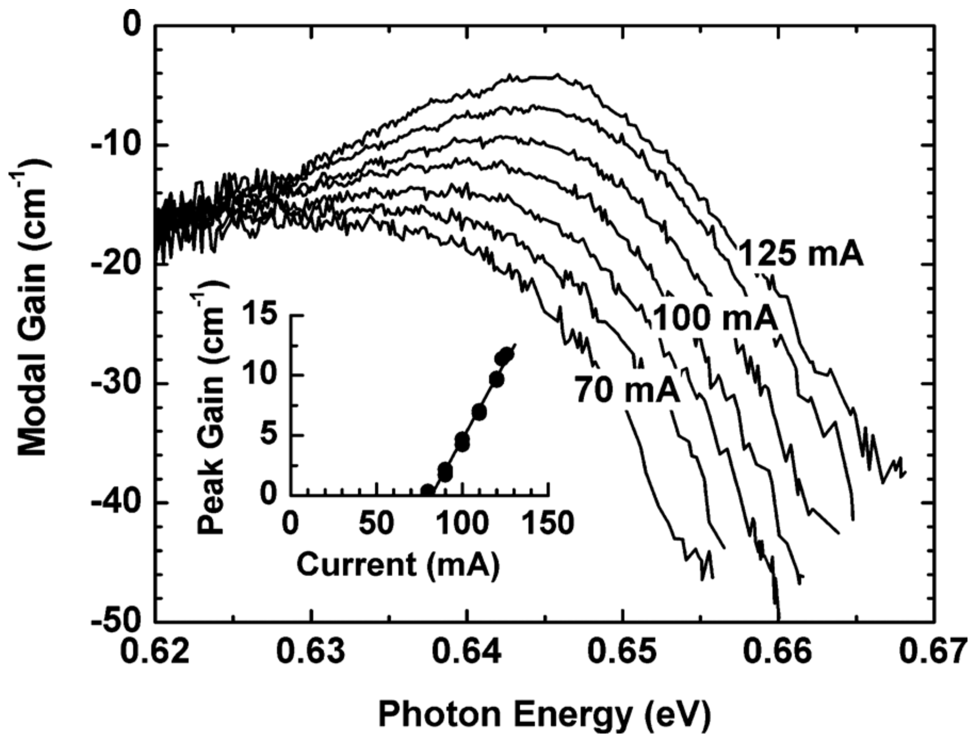

Figure 4.2.3 Modal gain spectra measured 200 ns/1 MHz at several currents below threshold for 1 mm long uncoated lasers. Inset shows the current dependences of peak modal gain.

Parameters T0≈80 K and T1≈250 K characterized exponential temperature

dependence of the threshold current and slope efficiency of 1 mm long uncoated devices in the temperature range from 15 to 50 ℃.

Figure 4.2.3 plots the modal gain spectra measured for 1 mm long uncoated lasers by Hakki–Paoli method supplemented with spatial filtering optics. Internal optical losses were estimated to be below 5 cm^{-1} (if mirror loss of 12 cm^{-1} is assumed). Relatively low value of the internal optical loss originates from the selective expansion of the optical field into n-cladding region while keeping its overlap with absorbing p-cladding below 4%. Internal efficiency about 85% was calculated from measured slope efficiency and optical loss. High level of the internal efficiency in combination with relatively low value of internal optical loss resulted into slope efficiency of the 3 mm long coated device of 0.25 W/A. Rate of increase in peak modal gain with current is about 250 cm^{-1} /A for 1 mm long lasers. Low transparency current density below 90 A/cm^2 (below 30 A/cm2 per QW) in combination with high differential gain resulted into cw threshold current density of about 110 A/cm^2 for high power lasers. Further reduction in the fast axis beam divergence is possible without dramatic penalty in device performance parameters. This can be achieved by reduction in the waveguide width in combination with reduction in the doping level of the n-cladding region.

4.2.4 Summary

In conclusion, 1.95 μm diode lasers with asymmetric claddings were designed and fabricated. Fast axis beam divergence of 42° was obtained in

transverse far field. Reduction in beam divergence was achieved by selective expansion of the optical mode into n-cladding region made of alloy with reduced band gap and increased refractive index. The heterobarrier leakage into cladding layers was inhibited by introduction of the carrier stopper layers. Temperature stable device performance indicated the effectiveness of the design approach chosen. Threshold current density of 110 A/cm^2 and external efficiency of 40% were demonstrated for 100 μm wide, 3 mm long, AR/HR coated high power lasers with about 1.5 W cw output power level at 20 ℃.

4.3 Appendix

4.3.1 For samples in chapter 4.1, the fabrication steps are the same as in Chapter 3

4.3.2 Fabrication steps for samples in chapter 4.2:

1. Etching (for making ridges)

   a. Lithography (Photoresist— AZ5214E-IR, Developer—351:H_2O=1:5)

      i. Spin— 4500 RPM for 30 sec

      ii. First bake—on hotplate at 85 ℃ for 120 sec

      iii. Exposure—10 mW/cm^2 for 15 sec

      iv. Second bake—on hotplate at 120 ℃ for 60 sec

      v. Exposure (flood)—10 mW/cm^2 for 45 sec

      vi. Develop—351:H_2O=1:5 for 60 sec

   b. Etching

      i. Solution

-Disolve Sodium hydrogentartrate, 98% (5 g) into H_2O (90 ml) and spin it for about 30 min

-Mix H_2O_2 (30 ml) and H_3PO_4 (30 ml) in the solution and leave it spin for at least 1 day

ii. Etching

-It will take 5~7 min for GaSb based materials to reach waveguide (GaSb Cap~50-100 nm, Graded~200 nm, $Al_{0.85}$GaAsSb p-clad~1500 nm, InAlGaAsSb WG~300-1000 nm)

-layer color eventually looks silver shiny after etching multiple layers of different colors (green, blue, etc.)

-remove photoresist completely (Aceton, Isopropanol, O_2 Plasma)

2. SiN deposition (Trion PECVD)

a. Sample preparation—HCl:H_2O=1:10 for 60 sec and dry with N_2 blast

b. Ar Plasma (300mT/100 W/250 ℃/Ar 40 sccm/300 sec)

c. NH_3 Plasma (300mT/100W/250 ℃/NH_3 40 sccm/600 sec)

d. Deposition (600 mT/50 W/250 ℃/DES 16 sccm/NH_3 16 sccm/N_2 160 sccm)

3. Open window

a. Lithography (Photoresist— NR1-3000PY, Developer—RD6)

i. Spin— 4000 RPM for 40 sec

ii. First bake—on hotplate at 130°C for 120 sec

iii. Exposure—10 mW/cm^2 for 33 sec

iv. Second bake—on hotplate at 110 ℃ for 80 sec

-layer color eventually looks silver shiny after etching multiple layers of different colors (green, blue, etc.)

-remove photoresist completely (Aceton, Isopropanol, O_2 Plasma)

v. Develop—RD6 for 27 sec

b. Open Window with PECVD (300mT/100W/room temperature/CF_4 35sccm/O_2 5 sccm/until open~600 sec)

4. First p-side metal deposition (Ti/Pt/Au by Temescal)

a. Sample preparation—NH_4OH:H_2O=1:20 for 20 sec and dry with N_2 blast

b. E-beam metal deposition (Temescal BJD)

i. Wait until the pressure going down below 1.0×10^{-6} Torr

ii. Turn on heat, set the chamber temperature at 70 ℃, and wait again for an hour or two

iii. Ar plasma for 60 sec (1.0×10^{-4} Torr/Ar ~3 sccm/Beam Voltage 500 V/40 mA)

iv. Wait till the chamber temperature cool down to room temperature

v. Deposition

-Ti (200 Å)/Pt (1000 Å)/Au (1000 Å)

vi. Liftoff—rinse with aceton to wash off photoresist

vii. O_2 plasma—160 mW for 60 sec $\times$3 times

5. Second p-side metal deposition (Ti/Au)

a. Lithography (Photoresist— NR1-3000PY, Developer—RD6)

i. Spin— 4000 RPM for 40 sec

ii. First bake—on hotplate at 130 ℃ for 120 sec

iii. Exposure—10 mW/cm^2 for 33 sec

iv. Second bake—on hotplate at 110 ℃ for 80 sec

v. Develop—RD6 for 27 sec

vi. O_2 plasma—160 mW for 60 sec $\times 3$ times

b. E-beam metal deposition (Temescal BJD)

i. Wait till the pressure going down below 1.0×10^{-6} Torr

ii. Turn on heat, set the chamber temperature at 70 ℃, and wait again for an hour or two

iii. Ar plasma for 60 sec (1.0×10^{-4} Torr/Ar ~3 sccm/Beam Voltage 500 V/40 mA)

iv. Wait until the chamber temperature cool down to room temperature

v. Deposition

-Ti (200 Å)/ Au (1000 Å)

vi. Liftoff— rinse with Aceton to wash off photoresist

vii. O_2 plasma—160 mW for 60 sec $\times 3$ times

6. Lapping and polishing

a. Lap down substrate to 100-130 µm (use 3-5 µm aluminum oxide powder)

b. Polish the surface—use solution of 20 nm TiC (5 ml)/Water (50 ml)/Clorox

(5-10 ml)

7. First n-side metal deposition (Ni/Au/Ge/Ni/Au)

a. Sample preparation—NH_4OH:H_2O=1:20 for 20 sec and dry with N_2 blast

b. E-beam metal deposition (Temescal BJD)

i. Wait till the pressure going down below 1.0×10^{-6} Torr

ii. Turn on heat, set the chamber temperature at 120 ℃, and wait again for an hour or two

iii. Ar plasma for 60 sec (1.0×10^{-4} Torr/Ar ~3 sccm/Beam Voltage 500 V/40 mA)

iv. Wait till the chamber temperature cool down to room temperature

v. Deposition

-Ni (50 Å)/Au (450 Å)/Ge (200 Å)/Ni (150 Å)/Au (2000 Å)

c. Rapid Thermal Processing (ramp 30 sec from room temperature to 250 ℃/stay at 250 ℃ for 120 sec)

-n-side metal layer diffuses in semiconductor and looks shiny white (becomes ohmic contact)

8. Second n-side metal deposition (Ti/Au)

a. Sample preparation—N_2 blast (dust off from surface)

b. E-beam metal deposition (Temescal BJD)

i. Wait till the pressure going down below 1.0×10^{-6} Torr

ii. Ar plasma for 60 sec (1.0×10^{-4} Torr/Ar ~3 sccm/Beam Voltage 500 V/40

mA)

iii. Wait till the chamber temperature cool down to room temperature

iv. Deposition

-Ti (200 Å)/Au (1000 Å)

4.3.3 LabView program for pulsed current-power measurement is the same as in chapter 2

4.3.4 LabView program for CW current-power-voltage measurement is the same as in chapter 3

V. Single Spatial Mode

5.1 Introduction

Lasers emitting near 3µm are needed for spectroscopic analysis of various chemical substances. For instance, the methane concentration in the planetary atmosphere can be analyzed by exploiting the CH_4 absorption feature near 3.27 µm. Single spectral mode diode lasers operating at room temperature in continuous-wave regime and providing mW level output power are required for development of the highly sensitive and compact tunable laser spectroscopy systems. Single mode type-I quantum-well (QW) GaSb-based diode lasers operating near 3 µm were previously reported [52]. The laser heterostructure comprised GaSb binary as a barrier material and corresponding ridge waveguide devices produced 7 mW at 15°C and operated up to 30°C in continuous-wave (CW) regime. Recently, the quinary AlInGaAsSb alloy was utilized as a barrier material, resulting in enhanced CW output power and operating wavelength of multimode broad stripe diode lasers [53, 54]. Here we report the design and development of single special mode GaSb-based type-I QW diode lasers employing quinary barrier material and operating in the spectral range near 3.15 µm. The ridge waveguide diode lasers produced 9 mW of CW output power at

3.16 μm at 15°C and had operating wavelength above 3.2 μm at 40°C. The introduction of the spectrally selective distributed feedback into the laser cavity will be a subject of separate work.

5.2 Laser heterostructure

The laser heterostructures were grown by solid source molecular beam epitaxy. In the laser active region there were three 1.65% compressively strained, 14 nm-wide, 40 nm-spaced InGaAsSb QWs with nominal indium composition of 52%. Quinary $Al_{0.20}Ga_{0.55}In_{0.25}As_{0.24}Sb_{0.76}$ alloy was utilized for the barrier and the waveguide. The width of the waveguide core from n-cladding to p-cladding was about 1120 nm. The n- and p-claddings were $Al_{0.85}Ga_{0.15}As_{0.07}Sb_{0.93}$ doped with tellurium and beryllium, respectively. The doping level of the part of the p-cladding layer adjacent to the waveguide was kept around 2×10^{17} cm^{-3} to reduce internal losses associated with free hole absorption.

5.3 Gain guided multimode lasers

For initial material characterization part of the wafer was processed into multimode gain-guided lasers by opening 100 μm-wide windows in the dielectric followed by flat metallization. No etching was performed at this stage to facilitate either optical or electrical lateral confinement. Laser mirrors were cleaved. Uncoated 1 mm-long lasers were mounted epi-side up for pulsed measurements. Figure 5.1 plots the light-current characteristics measured for minimum thermal

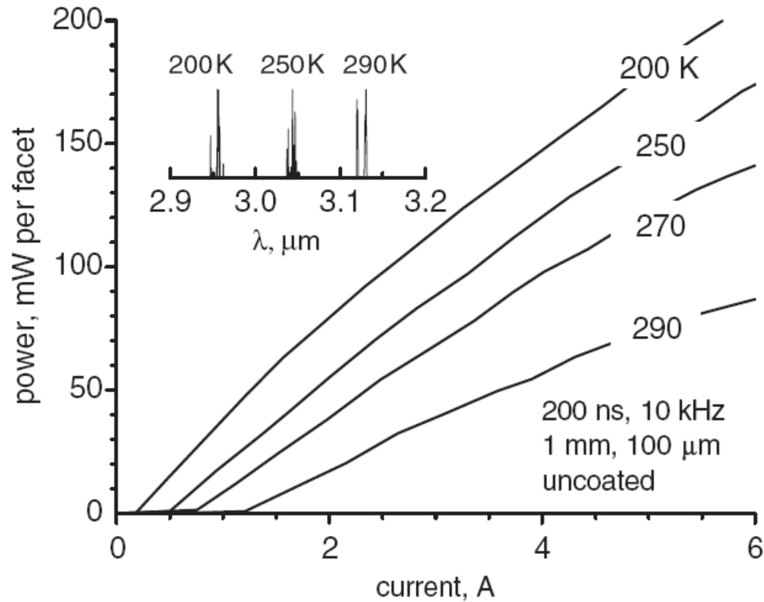

Figure 5.1 Temperature dependence of short pulse (200 ns, 10 kHz) light-current characteristics for 1-mm-long, 100-μm-wide, uncoated lasers.
Inset: Laser spectra

penalty in the short pulse regime at different heat-sink temperatures. The threshold current increases from below 200 mA to above 1 A when the device operating temperature increases from 200 to 290 K. The corresponding decrease of the laser slope efficiency is more than twofold. Strong temperature sensitivity of the lasers' slope efficiency contributes to the thermally activated increase of the laser threshold current. Poor thermal stability of laser external efficiency can originate either from internal optical loss increase or reduction of the injection efficiency with temperature. Unless free carrier absorption in active QWs is a dominant loss mechanism and/or QW carrier concentration is not pinned at

threshold neither of these effects are fundamental and, hence, the temperature stability of the laser threshold can be improved.

Measurement of the fast axis far-field distribution yielded divergence of 65° to 70° full-width-at-half-maximum (FWHM). Calculations using cladding refractive index of 3.2 [55] and waveguide refractive index guess of 3.8 produced far-field distribution with FWHM near 66°. Hence, one can conclude that 3.8 is the descent approximation for the quinary alloy refractive index and can be used for ridge waveguide design calculations.

5.4 Single spatial mode ridge lasers

Ridge waveguide lasers were fabricated using inductively coupled plasma (ICP) reactive ion etching technique. Very good control of the ridge sidewall has been achieved during dry etching as can be seen from the SEM image of the section of the ridge laser facet (Figure 5.2a). The etching was stopped at 350–400 μm before the end of the p-cladding to form shallow 12 μm-wide ridge lasers with an estimated lateral effective index step of about 0.0013. For such a small refractive index step the 12 μm-wide ridge waveguide is expected to support only fundamental mode. The ridge lasers were cleaved to form 2 mm-long cavities and coated to reflect about 30% (neutral-reflection) and above 90% (high-reflection), respectively. The distributed mirror losses of the coated 2 mm-long lasers are estimated to be about 3 cm^{-1}, i.e. lower than 12 cm^{-1} for 1 mm-long uncoated devices (Figure 5.1). Hence, the threshold carrier concentration is expected to be

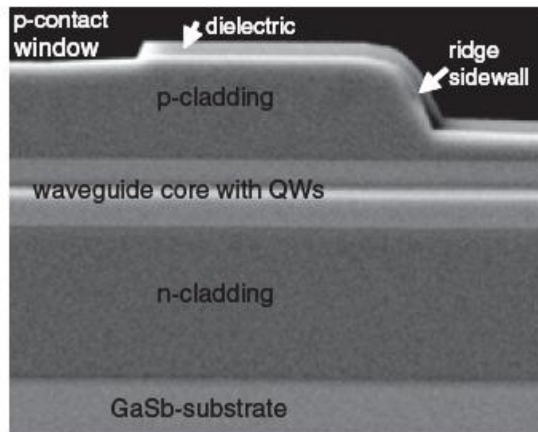

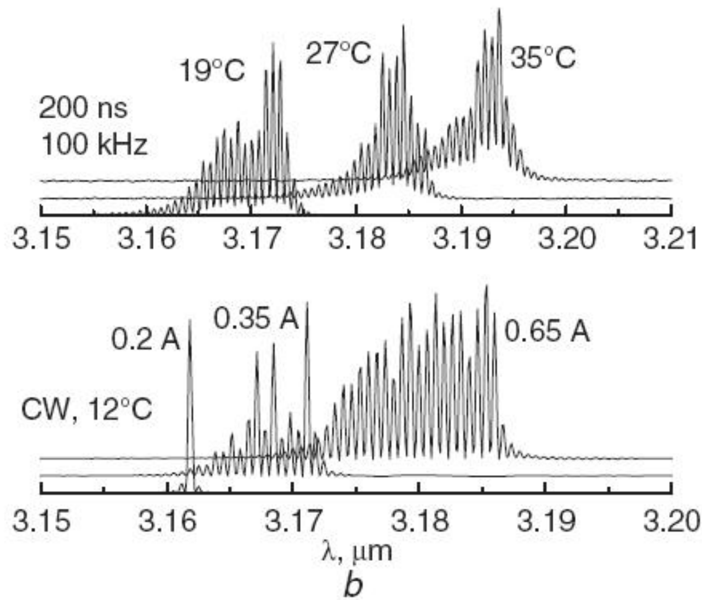

Figure 5.2 SEM image of front facet section of ridge waveguide laser, and ridge waveguide laser spectra measured in pulsed regime at different heatsink temperatures (top) and in CW regime at 12°C on heatsink. Spectra measured under different conditions shifted vertically for clarity

a. SEM image

b. Ridge waveguide laser spectra

reduced in ridge lasers (compared to test gain-guided devices) unless the ridge itself introduces extra losses. The devices were indium-soldered epi-side down on gold-coated polished copper blocks and characterized. Figure 5.2b plots the laser spectrum measured at different temperatures in pulsed mode (top) as well as current dependence of the CW spectrum at fixed heat-sink temperature (bottom). The ridge laser spectrum got shifted to longer wavelength compared to the reference gain guided lasers. The Figure 5.2b data allows estimation of the package thermal resistance as about 18 K/W. The values of the package thermal resistance we routinely obtain for 100 μm-wide 2 mm-long multimode lasers are about 2.5 K/W. Hence, one can conclude that thermal resistance for the devices with a ridge width in the range from 10 to 100 μm roughly scales with the ridge top area.

Figure 5.3 shows the light-current-voltage characteristics and slow axis far-field distribution measured at different temperatures. Lasers operate in continuous-wave regime up to 40°C with diffraction limited output beam. The slow axis far-field distribution remains nearly unchanged in the temperature range 15 to 40°C. The measured FWHM is between 9° and 10°. Model calculation predicted the FWHM about 9.4 for a given ridge etch. The agreement between the model and experiment is though the model ignored the possible effect of the absorption loss outside the ridge structure and associated imaginary index step.

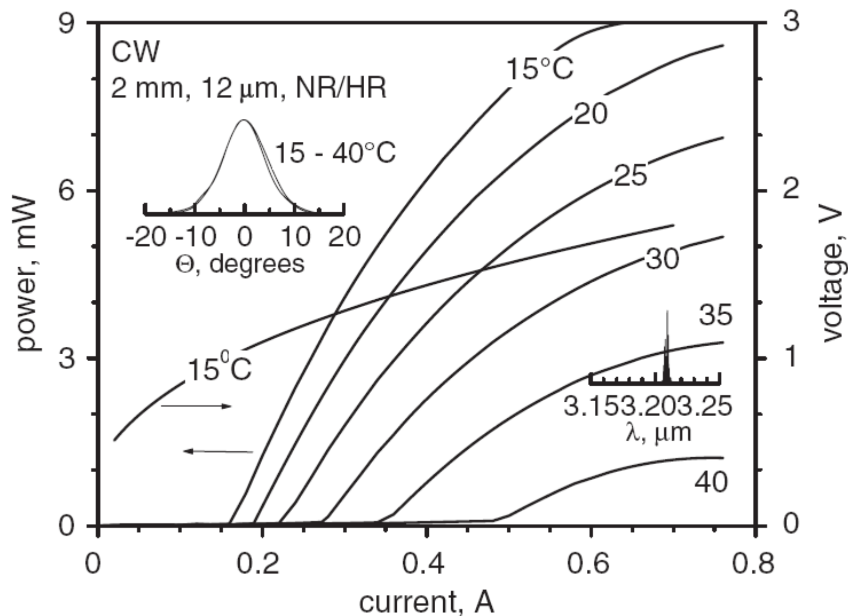

Figure 5.3 CW light-current-voltage characteristics measured for 12 μm-wide 2 mm-long ridge waveguide lasers in temperature range 15°C – 40°C
Inset: Slow axis far-field distributions measured at 15°C and 40°C.
Laser spectrum at 0.4 A of CW current at 35°C at heatsink also shown

Maximum power of 9 mW near 3.18 μm was achieved at the current of 0.65 A at heat-sink temperature of 15°C. The devices generate above 1 mW of CW power at heat-sink temperature of 40°C (the operating wavelength is above 3.2 μm, see inset to Figure 5.3). The CW threshold current density was about 700 A/cm^2 at 15°C, rising up to 2 kA/cm^2. The voltage drop across the laser heterostructure was below 2 V at the maximum output power level.

5.5 Conclusion

We designed and fabricated CW room temperature operated 3.1–3.2 μm GaSb-based diode lasers. Devices with a shallow ridge waveguide with total

width of 12 μm generate 9 mW of output power near 3.15 μm at 15°C with diffraction limited beam. Lasers mounted epi-down operate in CW up to above 40°C where they emit at a wavelength longer than 3.2 μm. Improvement of output power level, temperature stability and extension of the operating wavelength compared to previously reported results [52] was achieved thanks to utilization of the quinary InAlGaAsSb waveguide/barrier material facilitating hole confinement in active QWs.

5.6 Appendix

5.6.1 Fabrication steps for gain guided multimode lasers was the same as in chapter 4.2

5.6.2 Fabrication of 12 μm ridge waveguide single spatial mode lasers was done in Jet Propulsion Laboratory

5.6.3 LabView program for pulsed current-power measurement is the same as in chapter 2

5.6.4 Labview program for CW current-power-voltage measurement is the same as in chapter 3

Reference

[1] D.Z. Garbuzov, H. Lee, V. Khalfin, R. Martinelli, J.C. Connoly, G.L. Belenky, "2.3-2.7 um room temperature CW operation of InGaAsSb/AlGaAsSb broad waveguide SCH-QW diode lasers," *IEEE Photon. Technol. Lett.*, vol. 11, no. 7, pp. 794-796, Jul. 1999.

[2] S. Simanowski, N. Herres, C. Mermelstein, R. Kiefer, M. Walther, J. Wagner, G. Weinmann, "Strain adjustment in (GaIn)(AsSb)/(AlGa)(AsSb) QWs for 2.3-2.7 μm laser structures," *J. Crystal Growth*, vol. 209, no.1, pp. 15-20, Jan. 2000.

[3] Y. Rouillard, F. Genty, A. Perona, A. Vicet, D.A. Yarekha, G. Boissier, P. Grech, A.N. Baranov, C. Alibert, "Edge and vertical surface emitting lasers around 2.0-2.5 μm and their applications," *Phil. Trans. R. Soc. Lond. A*, vol. 359, no. 1780, pp. 581-597, Mar. 2001.

[4] J.G. Kim, L. Shterengas, R.U. Martinelli, G.L. Belenky, D.Z. Garbuzov, W.K. Chan, "Room-Temperature 2.5μm InGaAsSb/AlGaAsSb Diode Lasers Emitting 1W Continuous-Wave," *Appl. Phys. Lett.*, vol. 81, no. 17, pp. 3146-3148, Oct. 2002.

[5] M. Garcia, A. Salhi, A. Perona, Y. Rouillard, C. Sirtori, X. Marcadet, C. Alibert, "Low threshold high-power room-temperature continuous-wave operation diode laser emitting at 2.26 μm," *IEEE Photon. Technol. Lett.*, vol. 16, no.5, pp. 1253-1255, May. 2004.

[6] L. Shterengas, G.L. Belenky, A. Gourevitch, D. Donetsky, J.G. Kim, R.U. Martinelli, D. Westerfeld, "High-Power 2.3-μm GaSb-based Linear Laser Array," *IEEE Photon. Tech. Lett.*, vol. 16, no. 10, pp. 2218-2220, Oct. 2004.

[7] L. Shterengas, G. Belenky, M. Kisin, D. Donetsky, "High power 2.4 μm heavily strained type-I quantum well GaSb-based diode lasers with more than 1 W of continuous wave output power and a maximum power-conversion efficiency of 17.5%," *Appl. Phys. Lett.*, vol. 90, 011119, Jan. 2007.

[8] L. Shterengas, G. Kipshidze, T. Hosoda, J. Chen, G. Belenky, "Diode lasers emitting at 3 μm with 300 mW of continuous-wave output power ", *Electron. Lett.*, vol. 45, pp. 942-U37, Aug. 2008

[9] L. Shterengas, G. L. Belenky, J. G. Kim, R. U. Martinelli, "Design of high-power room-temperature continuous-wave GaSb-based type-I quantum-well lasers with λ > 2.5 μm," *Semicond. Sci. Tech.*, vol. 19, no.5, pp. 655-658, May. 2004

[10] T. Newell, X. Wu, A. L. Gray, S. Dorato, H. Lee, and L. F. Lester, "The effect of I increased valence band offset on the operation of 2μm GaInAsSb-AlGaAsSb lasers," *IEEE Photon. Technol. Lett.*, vol. 11, no. 1, pp. 30-32, Jan. 1999

[11] G.D. Sanders, Y.C. Chang, Phys. Rev. B 32, pp. 4282, 1985

[12] L. Shterengas, G. L. Belenky, J. G. Kim, R. U. Martinelli, "Design of high-power room temperature continuous-wave GaSb-based type-I quantum-well

lasers with λ > 2.5 μm," *Semicond. Sci. Tech.*, vol. 19, no.5, pp. 655-658, May. 2004

[13] T. Newell, X. Wu, A. L. Gray, S. Dorato, H. Lee, and L. F. Lester, "The effect of I increased valence band offset on the operation of 2μm GaInAsSb-AlGaAsSb lasers," *IEEE Photon. Technol. Lett.*, vol. 11, no. 1, pp. 30-32, Jan. 1999

[14] E. Yablonovitch, E. Kane, "Reduction of lasing threshold current density by the lowering of valence band effective mass," *IEEE Journal of Lightwave Technology*, vol. 4, no.5, pp. 504-506, May. 1986

[15] L. Shterengas, G. Belenky, M. Kisin, D. Donetsky, "High power 2.4 μm heavily strained type-I quantum well GaSb-based diode lasers with more than 1 W of continuous wave output power and a maximum power-conversion efficiency of 17.5%," *Appl. Phys. Lett.*, vol. 90, 011119, Jan. 2007

[16] D. Donetsky, G. Kipshidze, L. Shterengas, T. Hosoda, G. Belenky, "2.3-μm Type-I Quantum Well GaInAsSb/AlGaAsSb/GaSb laser diodes with a quasi-CW output power of 1.4 W," *IEE Electron. Lett.*, vol. 43, no. 15, pp. 810-812, Jul. 2007

[17] C. C. Largent, M. J. Grove, P. S. Zory, "Pulsed anodization technique for fabrication GaSb-based lasers," *SPIE Proceeding*, vol. 2382, pp. 244-249, Feb. 1995

[18] P. S. Zory, D. A. Hudson, M. J. Grove, "Method for producing Native Oxides on Compound Semiconductors", U.S. Patent 5 559 058, Sep. 24, 1996

[19] B.W. Hakki, T.L. Paoli, “Gain spectra in GaAs double-heterojunction injection lasers,” *J. Appl. Phys.*, vol. 46, pp. 1299-1306, Mar. 1975

[20] M.V. Kisin, "Modeling of the Quantum Well and Cascade Semiconductor Lasers using 8-Band Schrödinger and Poisson Equation System," in *COMSOL Conference 2007*, Newton, MA, USA, 2007, pp. 489-493

[21] I. Vurgaftman, J. R. Meyer, R. Mahan, "Band parameters for III-V compound semiconductors and their alloys," *J. of Appl. Phys.*, vol. 89, pp. 5815-5875, Jun. 2001

[22] G. P. Donati, R. Kaspi, and K. J. Malloy, "Interpolating semiconductor alloy parameters: Application to quaternary III-V band gaps," *J. of Appl. Phys.*, vol. 94, pp. 5814-5819, Nov. 2003

[23] S. Seki, T. Yamanaka, W. Lui, Y. Yoshikuni, and K. Yokoyama, "Theoretical Analysis of Pure Effects of Strain and Quantum Confinement on Differential Gain in InGaAsP/InP Strained-Layer Quantum-Well Lasers," *IEEE J. of Quantum Electronics*, vol. 30, pp. 500-510, Feb. 1994

[24] D. Botez, “Design considerations and analytical approximations for high continuous-wave power, broad-waveguide diode lasers,” *Appl. Phys. Lett.*, vol. 74, pp. 3102–3104, 1999

[25] J. G. K. L. Shterengas, R. U. Martinelli, and G. L. Belenky, “High power

room temperature continuous wave operation of 2.7 and 2.8 μm In(Al)GaAsSb/GaSb diode lasers," *Appl. Phys. Lett.*, vol. 83, pp.1926–1928, 2003

[26] M. Grau, C. Lin, and M. C. Amann, "Low threshold 2.72 μm GaInAsSb/ AlGaAsSb multiple-quantum-well laser," *Electron. Lett.*, vol.38, pp. 1678–1679, 2002

[27] M. Grau, C. Lin, O. Dier, C. Lauer, and M.-C. Amann, "Room-temperature operation of 3.26 μm GaSb-based type-I lasers with quinternary AlGaInAsSb barriers," *Appl. Phys. Lett.*, vol. 87, pp. 241104-1–241104-3, 2005

[28] T. Hosoda, G. Belenky, L. Shterengas, G. Kipshidze, and M. V. Kisin, "Continuous-wave room temperature operated 3.0 μm type I GaSb based lasers with quinternary AlInGaAsSb barriers," *Appl. Phys. Lett.*, vol. 92, pp. 091106-1–091106-3, 2008

[29] L. Shterengas, G. Belenky, T. Hosoda, G. Kipshidze, and S. Suchalkin, "Continuous wave operation of diode lasers at 3.36 μm at 12 degrees," *Appl. Phys. Lett.*, vol. 93, pp. 011103-1–011103-3, 2008

[30] R. Lewicki, G. Wysocki, A. A. Kosterev, and F. K. Tittel, "Carbon dioxide and ammonia detection using 2 μm diode laser based quartz enhanced photoacoustic spectroscopy," *Appl. Phys. B*, vol. 87, no. 1, pp. 157, 2007

[31] B. Jean and T. Bende, "Mid-IR laser application in medicine," in *Topics in Applied Physics*, vol. 89. Berlin/Heidelberg, Germany: Springer, pp. 530–

565, 2003

[32] M. Mond, D. Albrecht, E. Heumann, G. Huber, S. KucKück, V. Levchenko, V. Yakimovich, V. Shcherbitsky, K. Kisel, N. Kuleshov, M. Rattunde, J. Schmitz, R. Kiefer, and J. Wagner, "1.9µm and 2.0µm laser diode pumping of Cr:ZnSe and Cr:CdMnTe," *Opt. Lett.*, vol. 27, no. 12, p. 1034, 2002

[33] J. D. Wells, C. Kao, K. Mariappan, J. Albea, E. D. Jansen, P. Konrad, and A. Mahadevan-Jansen, "Optical stimulation of neural tissue in vivo," *Opt. Lett.*, vol. 30, no. 5, p. 504, 2005

[34] D. Z. Garbuzov, R. U. Martinelli, H. Lee, P. K. York, R. J. Menna, J. C. Connolly, and S. Y. Narayan, "Ultralow-loss broadened-waveguide high power 2 µm AlGaAsSb/InGaAsSb/GaSb separate-confinement quantum well lasers," *Appl. Phys. Lett.*, vol. 69, no. 14, pp. 2006–2008, 1996

[35] G. W. Turner, H. K. Choi, and M. J. Manfra, "Ultralow-threshold 0.50 A/cm^2 strained single-quantum-well GaInAsSb/AlGaAsSb lasers emitting at 2.05 µm," *Appl. Phys. Lett.*, vol. 72, no. 8, pp. 876–878, 1998

[36] D. Z. Garbuzov, R. U. Martinelli, H. Lee, R. J. Menna, P. K. York, L. A. DiMarco, M. G. Harvey, R. J. Matarese, S. Y. Narayan, and J. C. Connolly, "4W quasi-continuous-wave output power from 2mm AlGaAsSb/InGaAsSb single-quantum-well broadened waveguide laser diodes," *Appl. Phys. Lett.*, vol. 70, no. 22, pp. 2931–2933, 1997

[37] B. S. Ryvkin and E. A. Avrutin, "Free-carrier absorption and active layer

heating in large optical cavity high-power diode lasers," *J. Appl. Phys.*, vol. 100, no. 2, pp. 023104, 2006

[38] G. Belenky, L. Shterengas, D. Wang, G. Kipshidze, and L. Vorobjev, "Continuous wave operated 3.2μm type-I quantum-well diode lasers with the quinary waveguide layer," *Semicond. Sci. Technol.*, vol. 24, no. 11, pp. 115013, 2009

[39] M. Rattunde, J. Schmitz, G. Kaufel, M. Kelemen, J. Weber, and J. Wagner, "GaSb-based 2.x μm quantum-well diode lasers with low beam divergence and high output power," *Appl. Phys. Lett.*, vol. 88, no. 8, pp. 081115, 2006

[40] B. S. Ryvkin and E. A. Avrutin, "Nonbroadened asymmetric waveguide diode lasers promise much narrower far fields than broadened symmetric waveguide ones," *J. Appl. Phys.* vol. 98, no. 1, p. 026107, 2005

[41] A. Chandola, R. Pino, and P. S. Dutta, "Below bandgap optical absorption in tellurium-doped GaSb," *Semicond. Sci. Technol.*, vol. 20, no. 8, pp. 886, Aug. 2005

[42] Z. G. Li, G. J. Liu, M. H. You, L. Li, M. Li, Y. Wang, B. S. Zhang, and X. H. Wang, "2.0 μm room temperature CW operation of InGaAsSb/AlGaAsSb laser with asymmetric waveguide structure," *Laser Phys.*, vol. 19, no. 6, pp. 1230, 2009

[43] C. Alibert, M. Skouri, A. Joullie, M. Benouna, and S. Sadiq, "Refractive indices of AlSb and GaSb-lattice-matched $Al_xGa_{1-x}As_ySb_{1-y}$ in the

transparent wavelength region," *J. Appl. Phys.*, vol. 69, no. 5, pp. 3208–3211, 1991

[44] I. Vurgaftman, J. R. Meyer, and L. R. Ram-Mohan, "Band parameters for III–V compound semiconductors and their alloys," *J. Appl. Phys.*, vol. 89, no. 11, p. 5815, 2001

[45] S. Suchalkin, J. Bruno, R. Tober, D. Westerfeld, M. Kisin, and G. Belenky, "Experimental study of the optical gain and loss in InAs/GaInSb interband cascade lasers," *Appl. Phys. Lett.*, vol. 83, no. 8, pp. 1500–1502, 2003

[46] S. Suchalkin, D. Westerfeld, D. Donetski, S. Luryi, G. Belenky, R. Martinelli, I. Vurgaftman, and J. Meyer, "Optical gain and loss in 3 μm diode "W" quantum-well lasers," *Appl. Phys. Lett.*, vol. 80, no. 16, pp. 2833–2835, 2002

[47] T. Newell, X. Wu, A. L. Gray, S. Dorato, H. Lee, and L. F. Lester, "The effect of increased valence band offset on the operation of 2 μm GaInAsSb–AlGaAsSb lasers," *IEEE Photon. Technol. Lett.*, vol. 11, no. 1, pp. 30–32, Jan. 1999

[48] A. S. Kurkov, V. M. Paramonov, O. I. Medvedkov, Yu. N. Pyrkov, E. M. Dianov, S. E. Goncharov, and I. D. I. Zalevskii, Laser Phys. Lett. 3, pp. 151, 2006

[49] Alibert, M. Skouri, A. Joullie, M. Benouna, and S. Sadiq, J. Appl. Phys. **69**, pp. 3208, 1991

[50] Vurgaftman, J. R. Meyer, and L. R. Ram-Mohan, J. Appl. Phys. 89, pp.

5815 , 2001

[51] R. F. Kazarinov and G. L. Belenky, IEEE J. Quantum Electron. 31, pp. 423, 1995

[52] Lehnhardt, T., Hu ̈mmer, M., RoBner, K., Muller, M., Hofling, S., and Forchel, A., “Continuous wave single mode operation of GaInAsSb/GaSb quantum well lasers emitting beyond 3 μm”, Appl. Phys. Lett. 92, pp. 183508, 2008

[53] Shterengas, L., Kipshidze, G., Hosoda, T., Chen, J., and Belenky, G., “Diode lasers emitting at 3 μm with 300 mW of continuous-wave output power”, Electron. Lett., 2009, 45, p. 942

[54] Shterengas, L., Belenky, G., Hosoda, T., Kipshidze, G., and Suchalkin, S., “Continuous wave operation of diode lasers at 3.36 μm at 12 C,” Appl. Phys. Lett. 93, pp. 011103, 2008

[55] Alibert, C., Skouri, M., Joullie, A., Benouna, M., and Sadiq, S.: ‘Refractive indices of AlSb and GaSb-lattice-matched $Al_xGa_{1-x}As_ySb_{1-y}$ in the transparent wavelength region’, J. Appl. Phys. 69, pp. 3208, 1991